UNIVERSITY OF PISA

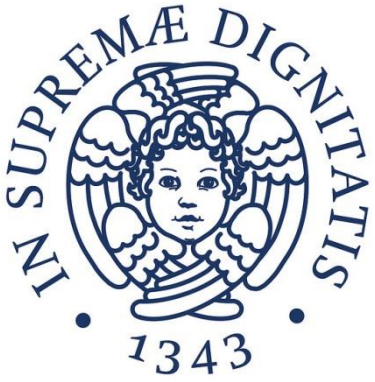

MSc THESIS IN NUCLEAR ENGINEERING

Calibration of a new spectrometry setup for in-vivo lung monitoring

CANDIDATE

Maria Luisa Allegrini

SUPERVISORS

Riccardo Ciolini (University of Pisa)

Anne Laure Lebacq (SCK-CEN)

Academic year 2015/2016

INDEX

Index of figures ..... **iv**
Index of tables ..... **vii**
Introduction **1**
1 Semiconductor detectors and Gamma spectrometry **3**
1.1 Structure 3
1.2 Radiation interaction 4
1.3 High Purity Germanium detectors (HPGe) 7
1.3.1 Detector manufacturing *7*
1.3.2 Configurations *8*
1.3.3 Operational characteristics *9*
1.3.4 Gamma spectroscopy [2] *10*
1.3.5 Effects on detector performance [2] *12*
1.4 Gamma spectrometry 13
1.4.1 Detector response function *13*
1.4.2 Energy calibration *14*
1.4.3 Resolution calibration *15*
1.4.4 Efficiency calibration *17*
2 Anthropogammametry **20**
2.1 General features 20
2.2 In-vivo monitoring 20
2.3 Internal dosimetry 21
2.3.1 Human respiratory tract model *22*
3 SCK-CEN Anthropogammametry Laboratory **25**
3.1 General features 25
3.2 Preparation to the the measurements 25
3.3 Bunker structure 26
3.4 Whole body counting 27
3.5 Actual setup for lung monitoring 28
3.6 New setup for lung monitoring 29
4 Gamma spectrometry for lung monitoring **32**

4.1 Introduction 32
4.2 Background measurements 32
4.3 Energy and Resolution Calibration 35
4.3.1 Sources 35
4.3.2 Results for 4k channels 35
4.3.3 Results for 8k channels 39
4.4 Quality Assurance measurements 42
4.4.1 Radioactive sources 42
4.4.2 Protocol for QA measurements 42
4.4.3 Results 43
4.5 Efficiency calibration 45
4.5.1 Lawrence Livermore National Laboratory (LLNL) phantom 45
4.5.2 Counting protocol 46

5 MCNP simulations for efficiency 48
5.1 Introduction 48
5.2 LLNL Phantom and HPGe detectors 48
5.2.1 Models 48
5.2.2 Validation of the model 50
5.2.3 Best position 51
5.2.2 Comparison with measurements 53

6 Measurements results: efficiency curves 55
6.1.1 Comparison with actual setup 57

7 Uncertainties analysis and Detection limits 59
7.1 Introduction 59
7.2 Counting uncertainties 59
7.3 Efficiency uncertainties 61
7.4 Source activity uncertainties 65
7.5 Uncertainty in the chest wall thickness 66
7.6 Uncertainty in efficiency curve fitting 66
7.7 Sum of the uncertainties 66
7.8 Other uncertainties with MCNP 67
7.8.1 Anthropomorphic phantom model 67
7.8.2 Validation 68

7.8.3 Uncertainties tests 69
7.9 Detection limits 73

Conclusions 76
References 78
Acknowledgments.....81

Index of figures

Figure 1.1: generation of electron/holes pairs in a semiconductor 4
Figure 1.2: reverse polarization in semiconductor detectors 6
Figure 1.3: germanium detector overview [2] 9
Figure 1.4: typical gamma ray spectrum for Germanium detector [2] 11
Figure 1.5: ^{60}Co gamma ray spectrum for germanium detectors of three different sizes with the relative efficiencies (see paragraph 1.4.4) shown [2]. 12
Figure 1.6: intermediate detector size spectrum [2]. 14
Figure 1.7: energy calibration curve in *Genie 2000 Gamma Spectrometry Software from Canberra* 15
Figure 1.8: comparative pulse height spectra recorded using sodium iodine scintillator and Ge(Li) detector. [2] 16
Figure 1.9: definition of detector resolution [2] 16
Figure 1.10: resolution calibration from Genie 2000 Gamma Spectrometry Software from Canberra 17
Figure 1.11: efficiency calibration curve from *Genie 2000 Gamma Spectrometry Software from Canberra* 19
Figure 2.1: main routes in intake, transfers and excretion of radionuclides in the body [8] 22
Figure 2.2: human respiratory tract [8] 23
Figure 2.3: compartment model representing particle transport from each respiratory tract region Values alongside the arrows represent the fraction retained in the various parts [8]. 24
Figure 3.1: counter for external contamination (hands and feet) 25
Figure 3.2: bunker overview 26
Figure 3.3: NaI detector for whole Body Counting 27
Figure 3.4: BEGe detector for thyroid monitoring 28
Figure 3.5: LEGe detectors for lung monitoring 29
Figure 3.6: ORTEC detector for lung monitoring 30
Figure 4.1: background spectra for 4K setup (Sum of three) 34
Figure 4.2: background spectra for 8k setup (Sum of three) 34
Figure 4.3: blue detector energy calibration curve (4k setup) 36

Figure 4.4: blue detector FWHM curve (4k setup) 36
Figure 4.5: green detector energy calibration curve (4k setup) 37
Figure 4.6: green detector FWHM curve (4k setup) 37
Figure 4.7: red detector energy calibration curve (4k setup) 38
Figure 4.8: red detector resolution curve (4k setup) 38
Figure 4.9: blue detector energy calibration curve (8k setup) 39
Figure 4.10: blue detector FWHM curve (8k setup) 39
Figure 4.11: green detector energy calibration curve (8k setup) 40
Figure 4.12: green detector FWHM curve (8k setup) 40
Figure 4.13: red detector energy calibration curve (8 setup) 41
Figure 4.14: red detector FWHM curve (8k setup) 41
Figure 4.15: sources of ^{241}Am and ^{152}Eu used for QA 42
Figure 4.16: holder used for QA sources 42
Figure 4.17: red detector FWHM in QA check 44
Figure 4.18: red detector decay corrected area check for QA 44
Figure 4.19: LLNL phantom overview 45
Figure 4.20: overlays of LLNL phantom with different chest wall thicknesses 45
Figure 4.21: position with 2 detectors 47
Figure 5.1: wiew of LLNL phantom from *Moritz* 49
Figure 5.2: view of detector from *Moritz* 50
Figure 5.3: validation of the model 50
Figure 5.4: graph of the efficiency depending on the position 51
Figure 5.5: best position for three detectors 52
Figure 5.6: best position for two detectors 53
Figure 5.7: difference between MCNP simulations and measurements 54
Figure 6.1: efficiency at low energy (up 121 keV) 55
Figure 6.2: efficiency curves for different CWT. 56
Figure 6.3: efficiency curves trend in *Genie2000* 57
Figure 6.4: comparison between HPGe and LEGe efficiency curves 58
Figure 7.1: uncertainties changing the distance between detectors and chest for CWT0 62
Figure 7.2: uncertainties changing the distance between detectors and chest for CWT4 62
Figure 7.3: uncertainties changing the height of the detectors for CWT0 63

Figure 7.4: uncertainties changing the height of the detectors for CWT4 64
Figure 7.5: uncertainties changing the position of the phantom to the right and to the left for CWT0..... 64
Figure 7.6: uncertainties changing the position of the phantom to the right and to the left for CWT4..... 65
Figure 7.7: view of new phantom from *Moritz* 68
Figure 7.8: validation of the anthropomorphic model..... 68
Figure 7.9: position of two detectors for validation 68
Figure 7.10: change of the distance between the detectors and the chest. Above Red and green detector, below blue detector. 70
Figure 7.11: change of the lung size. Above the size is bigger, below is smaller..... 71
Figure 7.12: relative efficiency changing the distance between detectors and chest 72
Figure 7.13: relative efficiency changing lungs size 72

Index of tables

Table 1: Regional deposition of inhaled 5µm AMAD in Reference Worker [8] 24
Table 2: List of background peaks 33
Table 3: calibration sources for energy calibration 35
Table 4: peaks used for calibration 35
Table 5: Energy peaks used for QA check 43
Table 6: LLNL phantom data 46
Table 7: Peaks used for efficiency calibration 47
Table 8: Phantom composition 49
Table 9: Validation data 51
Table 10: Repetition uncertainties 60
Table 11: Sum of the uncertainties (in the second column the uncertainty was divided for the appropriate distribution coefficient) 67

INTRODUCTION

The Anthropogammametry Laboratory of SCK-CEN has the objective to screen workers of nuclear facilities (SCK-CEN and other companies) for internal contamination, because they can be contaminated from inhaling or swallowing radioactive material.
Routine measurements, carried out daily, are:

- Whole body counting: measurements of the activity in the total body with a big NaI scintillator;
- Lung monitoring: measurements of the activity in the lungs with two LEGe (Low Energy Germanium) detectors.

In lung monitoring, the objective is to screen if plutonium has been inhaled from the people and, to do this, ^{241}Am peak energy (59 keV) is searched by using three germanium detectors, which are chosen for their high resolution, especially at low energy. To increase the measurement efficiency a new set of bigger Germaniun detectors were mounted in the SCK-CEN anthropogammametry laboratory.

The objective of this study is to calibrate and optimize this new setup for in-vivo lung monitoring based on a system of three new HPGe (High Purity Germanium) detectors. Finding the best position of the detectors and evaluating the measurements uncertainties will lead to an improvement of the detection efficiency which automatically reduce the MDA (Minimum Detectable Activity) that can be detected in the worker lungs.

The Monte Carlo code will be the tool to find the measurement position in order to reach the best efficiency of the detectors. For the calibration of the detectors, a physical phantom (Livermore Lawrence National Laboratory phantom) will be used. Because the efficiency changes a lot with the thickness of the chest at low energy (range of our interest), this phantom is provided with four overlays of different Chest Wall Thickness (CWT).

After doing the measurements with this phantom, different efficiency curves depending on the CWT will be obtained. They will be implemented in the used software (*Genie2000*) and in this way, when a person arrives for his measurement, it will be possible to choose the suitable curve, depending on its CWT.

Also efficiency uncertainties analysis will be done, because there will be several parameters that could affect the reliability of the measurements, like the movements of the people during the measurements. MCNP will be also used for studies about the efficiency differences that can be present changing some parameters, like distance between detectors and torso and lungs size.

1 SEMICONDUCTOR DETECTORS AND GAMMA SPECTROMETRY

1.1 Structure

Semiconductor detectors have a better energy resolution than scintillators, together with a compact size and fast timing characteristics. On the other side, they can undergo radiation-induced damage at high energy, which could degrade their performances, and they are also really expensive. Among the semiconductor materials, the most available is silicon, used for charged particle spectroscopy. For gamma rays, instead, germanium is preferred.

The periodic structure of the crystalline material allows energy bands for electrons inside the material. The lower band, indicated as valence band (E_v), is composed of electrons which are bounded to lattice sites inside the crystal while the upper band, denoted as conduction band (E_c), is characterized by the presence of free electrons which contribute to the material conductivity. These two bands are separated by a band of forbidden states named band gap (whose amplitude is about 1 eV for semiconductor materials). The band gap dimension defines the classification of material as conductor, semiconductor or insulator. In absence of thermal excitation, semiconductor exhibits a valence band full of electrons while conduction band is totally empty. If an energy exceeding the band gap energy is imparted to an electron located in the valence band, this electron can be transferred to the conduction band and a vacancy (called hole) is created inside the valence band. The average displacement of a movable charge carrier due to thermal random motion is zero but owing to the application of an electrical field, both the electron within the conduction band and the hole inside the valence band (which represents a positive charge) can move contributing to the material conductivity. Because of electrons are drawn in a direction opposite to the electric field, holes move in the same direction as the electric field [1].

Alteration of semiconductor lattice structure is obtained adding a small amount of other elements with a different atomic structure (called impurities). This procedure, which can be performed either during crystal growth or later, is called doping. When impurity elements, dopants, are added to the semiconductor material, their impurity atoms substitute the semiconductor atoms in the lattice structure. If impurity atoms have one more valence electron than the semiconductor atom, this extra electron cannot form an

electron pair bond because no adjacent valence electron is available, then it requires only slight excitation energy to break away. Consequently, the presence of such excess electrons increases the semiconductor conductivity. The resulting material is called *n-type* semiconductor because the excess free electrons have a negative charge and the impurities of this type are referred to as donor atoms. In this case, electrons are called majority carriers and holes minority carriers.

A different effect is produced when impurity atoms, having one less valence electron than the semiconductor atom, are substituted in the lattice structure. Although all the valence electrons of the impurity atoms form electron pair bonds with electrons of neighbouring semiconductor atoms, one of the bonds in the lattice structure can not be completed because the impurity atom lacks the final valence electron. As a result, a vacancy (hole) exists in the lattice and an electron from an adjacent electron pair bond may absorb enough energy to break its bond and to fill the hole. As in the case of excess electrons, the presence of holes encourages the flow of electrons in the semiconductor material with a consequent increasing of the material conductivity. Semiconductor of this type, having an excess of holes, is called *p-type* semiconductor and the adopted impurities are indicated as acceptor atoms（Figure 1.1).

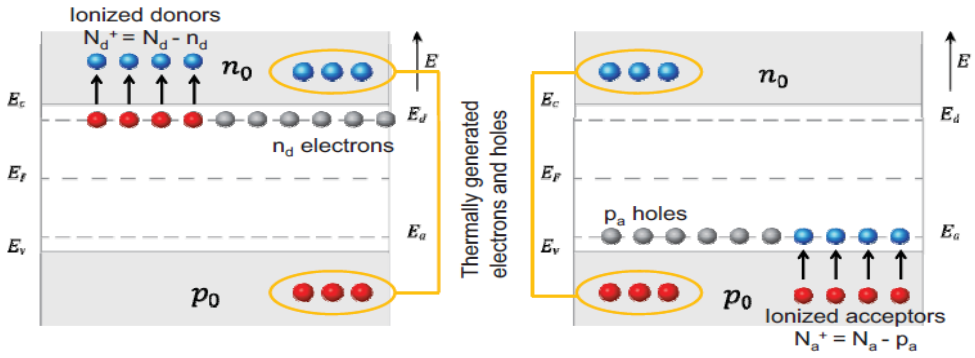

Figure 1.1: generation of electron/holes pairs in a semiconductor

1.2 Radiation interaction

The Radiation interaction with semiconductor materials creates electron-hole pairs that can be detected as electric signal. In presence of uncharged radiations, such as gamma - ray, photons have first to undergo an interaction with a target electron or with the semiconductor nucleus. The average energy converted into electron/hole pair creation, called ionization energy, is specific of the particular absorbing material and it is weakly

dependent on the type and energy of the incident radiation, except that for low energies comparable with the semiconductor band gap. This characteristic allows the interpretation of the number of produced electron/hole pairs produced in terms of the radiation incident energy. The ε-value for silicon and germanium is about 3 eV, ten times lower than the typical value of gas detector; then, for an absorbed energy E, an increased number of charge carriers is produced in Si or Ge detectors. The mean number of generated pairs N is obtained with the expression: $N = \frac{E}{\varepsilon}$.

After the electron/ hole generation inside the semiconductor, the created charges will tend to migrate spontaneously or due to an electrical field application. Their motion will continue until they are collected at the corresponding electrodes or they recombine because of the presence of impurities or structural imperfections inside of the detector material. Recombination produces an incomplete charge collection. In particular, impurities inside the semiconductor act as traps because they introduce additional energy levels inside the forbidden gap (deep impurities). These levels could capture electrons or holes and they release them after a time period. If the trapping time is long, the captured carriers cannot contribute to the measured pulse. In addition, structural defects within the crystal structure of the semiconductor can lead to trapping phenomenon and charge carrier loss. The usefulness of semiconductors as electronic circuit elements and radiation measurement stems from the special properties obtained when n and p type semiconductors are brought into good thermodynamic contact creating a diode junction. A junction is built by diffusing acceptor impurities into a n type silicon crystal or by diffusing donor atoms into a p type silicon crystal. A charge depleted region occurs at the interface of the n and p type regions. The result of both electron diffusion from n type material into p type and hole diffusion from p type to n type material. Therefore, diffusion is responsible for the existence of a space charge region composed of two zones: a first zone made of filled electron acceptor sites not compensated by hole and a second zone made of positively charged empty donor sites not compensated by electrons (Figure 1.2).

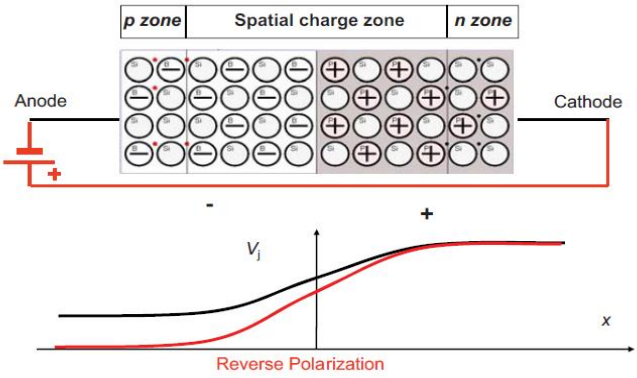

Figure 1.2: reverse polarization in semiconductor detectors

The space charge creates an electrical field that reduces the tendency for further diffusion. At equilibrium, the field is adequate to prevent additional net diffusion across the junction and a steady state charge distribution is therefore established. Therefore, the depletion region acts like a high resistivity parallel plate ionization chamber, making it feasible to use the diode junction for radiation detection. Due to the electric field, electron/hole pairs produced within the depleted region migrate out and their motion gives rise to an electrical signal. For this reason, the depletion region represents the sensitive volume of the semiconductor detector. Unbiased p-n junction can act like a detector but only with very poor performance because the depletion region thickness is small, the junction capacitance is high and the electric field strength across the junction is low and not enough to collect the induced charge carriers that, consequently, could be lost due to trapping and recombination. The performance of the p-n junction as a radiation detector is improved by applying an external voltage that leads the junction to be reversed biased. As the applied voltage raises, both the width of the depletion region increases, the junction capacitance decreases and the detection performance improves. Semiconductor detectors thus operate with a reverse bias voltage that can produce either a space charge region contained within the interior volume of the wafer (partially depleted detector) or a space charge region that extends throughout the full wafer thickness (fully depleted detector). However, the applied voltage should always be kept below the breakdown voltage of the detector so to avoid a deterioration of the detector properties.

The thickness of the depletion region *d* is calculated as [2]:

$$d = \left(\frac{2\epsilon V}{eN}\right)^{1/2} \qquad \text{(Eq. 1)}$$

Where:

V= reverse bias voltage

N= net impurity concentration

ϵ= dielectric constant

e= electronic charge

Using Silicon or Germanium of normal purity, a depletion zone of few millimetres can be reached. If the voltage is fixed, lowering the N value, that is decreasing the impurities, is the only choice to increase the depletion zone. To do that it is possible to produce a High Purity Germanium detector or to create a compensed material in which the impurities are balanced by other dopants.

1.3 High Purity Germanium detectors (HPGe)

1.3.1 Detector manufacturing

The initial starting material is zone refined in a quartz "boat" having a pyrolytic graphite coating. The germanium is melted in a crucible using radio frequency (RF) heating coils. A zone refiner uses the principle that most impurities concentrate in the liquid phase as the material begins to freeze. As the RF coils are slowly moved along the length of the crucible, the molten zone moves with them. Thus, the germanium melts as the coil approaches and freezes as the coil moves away. The ingot is continuously melted at the advancing solid-liquid interface and freezed at the receding interface. The impurities tend to remain in the molten section and hence are "swept" to one end of the ingot by this process. This "sweeping" operation is repeated many times, until most of the impurities are concentrated at one end of the ingot. This end is then removed, leaving the remaining portion much purer than the original starting material. The reduction in impurity concentration actually realized is about a factor of 100 or more at the completion of this process. The impurity concentration of the remaining portion is then determined by a Hall Effect measurement, and the ingot is sliced into pieces suitable for loading into the crystal-growing equipment. Crystals of germanium are grown using the Czochralski technique. A precisely cut seed crystal is dipped into the molten germanium and then withdrawn slowly, while maintaining the temperature of the melt just above the freezing

point. The rate of crystal withdrawal and temperature of the melt are adjusted to control the growth of the crystal. High-purity germanium crystals suitable for detector fabrication are usually grown in a quartz crucible under a hydrogen atmosphere. Near the completion of the growth process, the crystal is tapered gradually at the tail to minimize thermal strain. Sections of the crystal from both top and bottom are checked by Hall effect measurements to determine the impurity concentration and type (n or p). On this basis, that part of the crystal, which contains detector-grade material, is selected. The section of crystal, which has both adequate purity and crystallographic perfection for coaxial detector fabrication, is then ground perfectly cylindrical [3].

1.3.2 Configurations

A thickness of at least 5 cm is needed for having efficient detection, because of the photon mean free path in the material. Maximum depletion depth is less than 1 or 2 cm. There are two typical configurations for this type of detector: planar and coaxial.

In a planar configuration, the electric contacts are connected to two flat surfaces of a germanium crystal. The depletion zone is formed by reverse biasing n^+ (with diffusion of lithium)-p^+ (with implantation of boron) junction. High voltage is applied to the n^+ contact and the depletion zone is formed in the region near this contact. When the voltage raises, it expands in the p-side. Once the detector is full, the voltage makes a strong electric field that shortens carrier collection times and reduces the risk of carrier losses. Planar configurations can be fabricated also starting with n-type crystal.

In a coaxial configuration one electrode is fabricates at the outer surface of a cylindrical crystal and the other electrode is located at the inner surface of the central hole. Therefore, it is possible to have a large active volume. The most common configuration is the closed-ended coaxial. To make the p-n junction at the outer surface, the n+ contact is performed over the outer surface for a p-type detector while the p+ contact is applied in case of an n-type crystal. The n-type coaxial detectors are often called reverse electrode detectors. The reverse bias requires a positive outside potential for a p-type and a negative potential for an n type relative to the central electric potential. Regardless of the crystal type, a coaxial detector can be used for general gamma-ray spectroscopy purposes. For low energy gamma-rays below 100 keV, a significant portion of the incident photons is attenuated for p-type detectors due to the relatively thick surface dead layer. Thus, p-type coaxial detectors are normally limited down to 50 keV. Since the dead layer thickness of n-type detectors is much thinner, n-type detectors are still effective for low energy

photons (down to several keV) when coupled to a thin Be entrance window. Therefore, n-type detectors cover quite a wide spectral region compared to p-type coaxial and planer detectors [2].

1.3.3 Operational characteristics

The leakage current at room temperature could be too high and this could increase the noise and then make the resolution worse. For this reason germanium detectors have to be cooled, normally at 77 K. Usually a dewar with a reservoir of liquid nitrogen is present, but also electrical coolers can be used (Figure 1.3).

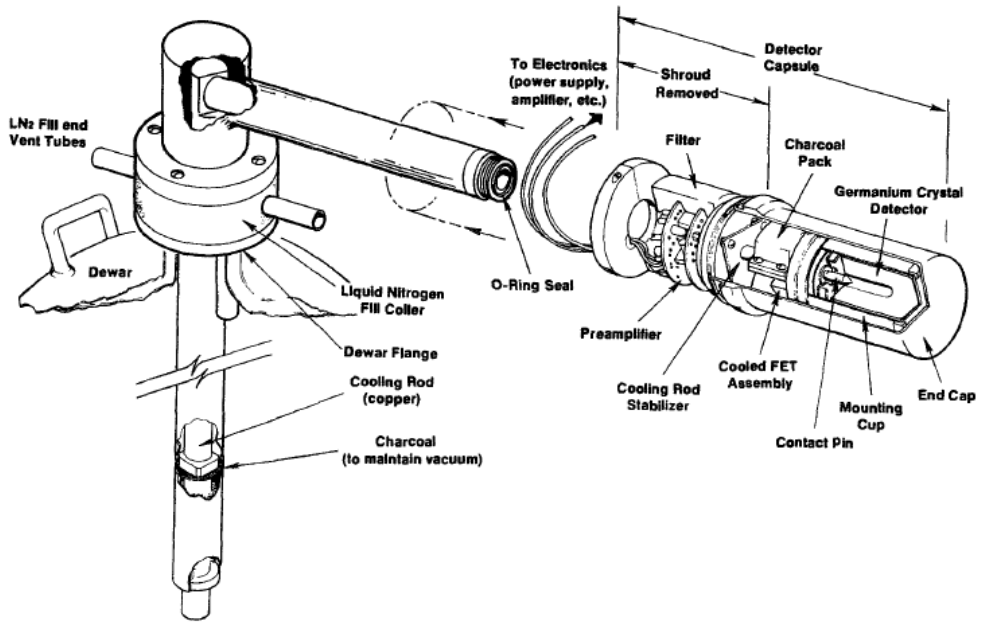

Figure 1.3: germanium detector overview **[2]**

The detectors have to be placed in a vacuum-tight cryostat that is evacuated and sealed by the manufacturer. The vacuum is needed for the thermal conductivity between the cryostat and the surrounding air. Furthermore they have an interlock that blocks the application of high voltage, if the temperature is not enough low.

When semiconductor detectors are used as spectrometers, they are connected to a charge-sensitive preamplifier with a high dynamic input capacitance. This preamplifier integrates on the capacitance the current signal from the detector and feeds the voltage signal to the main amplifier.

Motion of the charge carriers created by the ionizing radiation induces on the contact of the detector the current delivered by the signal generator. It is possible to calculate the electric field E knowing applied bias voltage, detector geometry and resistivity. Once E

is known, the motion of a charge carriers at a given point can be calculated trough the values of the drift velocity as a function of the electric field [2].

The rise time of the pulse generated by the detector is another important parameter. The main factor that influences this time is the charge collection time that can be calculated, for germanium detector at nitrogen liquid temperature, as

$$TR \cong W * 10^{-8} s \qquad \text{(Eq. 2)}$$

Where W is the thickness of the depletion region measured in mm. This value is provided for each detector.

This formula gives only the order of magnitude, not the exact value.

Furthermore, trapping effects have to be considered. These effects happen when the carrier is captured by an impurity and it is temporarily lost. Then we have to introduce the mean free drift time τ^+ that is dependent by the density of trapping centers trapping cross section and thermal velocity. However, the trapped charge carriers can be reemitted in the band and take part again in the transport process: the average time spent in a trap is the detrapping time τ^D and is dependent on the temperature.

If this value is of the same order of magnitude of the electronic shaping constants, the charge carrier is lost and the result is poor resolution and peak tailing.

In the actual germanium gamma-ray spectrometer the charge collection efficiency is of the order 0.999 and τ^+ is of the order of 10^{-4} s (Versus $\tau^D = 10^{-7}$ s).

1.3.4 Gamma spectroscopy [2]

Gamma rays interact in Ge detectors by photo absorption, Compton scattering or production of electron–positron pairs (for details see [2]). The fast electrons and positrons created by these processes are stopped in the detector by electron scattering producing electron–hole pairs. In the electric field of the Ge diode, the electrons move to the n+-contact while the holes move to the p+-contact. As the charge, carriers move they induce a current on the contacts. The shape of the detector signal depends on the electric field strength, the electron and hole drift velocities and the distance of the photon interaction from the contacts [4]. As said before, the advantage of these type of detectors is the improved energy resolution, even if this decreases the efficiency.

The typical pulse height spectra measured with a germanium detector is given in Figure 1.4. Photoelectric absorption, Compton Effect and pair production are all present. Germanium has a lower atomic number than sodium iodine and for this reason, the photoelectric cross section is smaller than sodium iodide scintillator, so the intrinsic peak efficiency results smaller. Even if this area is small, the full-energy peak is really narrow, because of the better energy resolution. Moreover, also the continuum Compton is an important effect to take into account in the germanium detector spectrum.

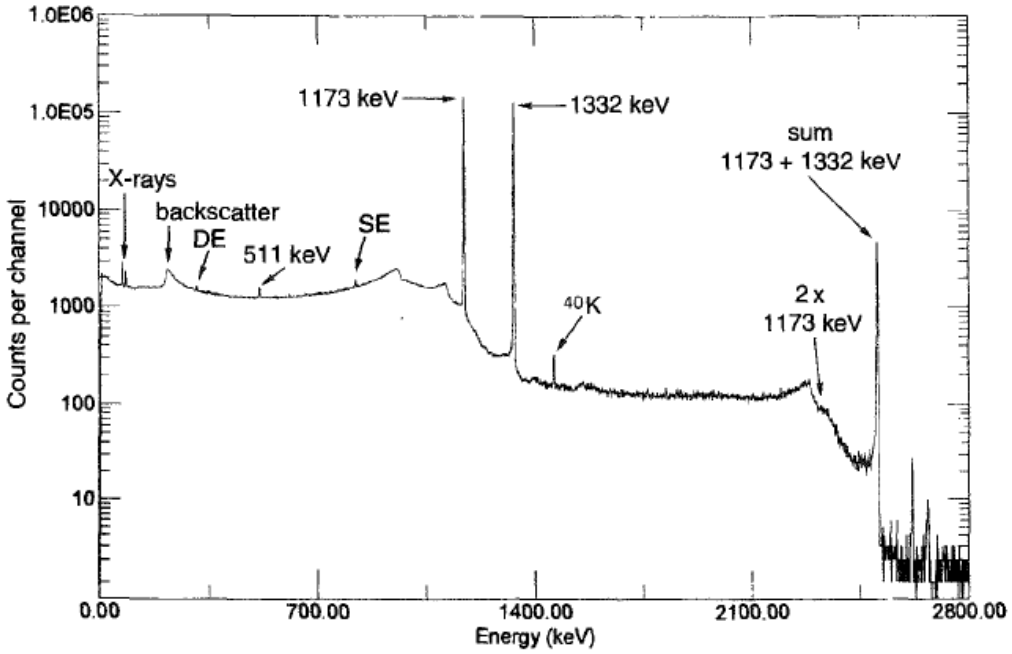

Figure 1.4: typical gamma ray spectrum for Germanium detector **[2]**

These detectors have a high transparency to secondary gamma rays, so escape peaks are really important. Escape peaks are made when a fixed amount of energy may be lost from the detector with high probability. X-ray escape is the most prominent effect that could happen, especially for incident low-energy gamma rays.

For high-energy gamma rays, instead, annihilation radiation following pair production is really significant. Escape peaks will appear in the spectrum when one or both of the annihilation photons carry away a part of the original gamma energy. If both annihilation photon escape, we can see a double escape peak in the spectrum; its energy is equal to 1.022 MeV less the full-energy peak. For a single escape, instead, we can see a peak with energy equal to 0.511 MeV less the full-energy peak.

Germanium detectors of a few millimetres thickness are often applied in the low-energy range. In the figure below (Figure 1.5), it is possible to see typical germanium spectra, also for larger volume detectors. The Compton continuum decreases if the detector volume and then the detector efficiency increases.

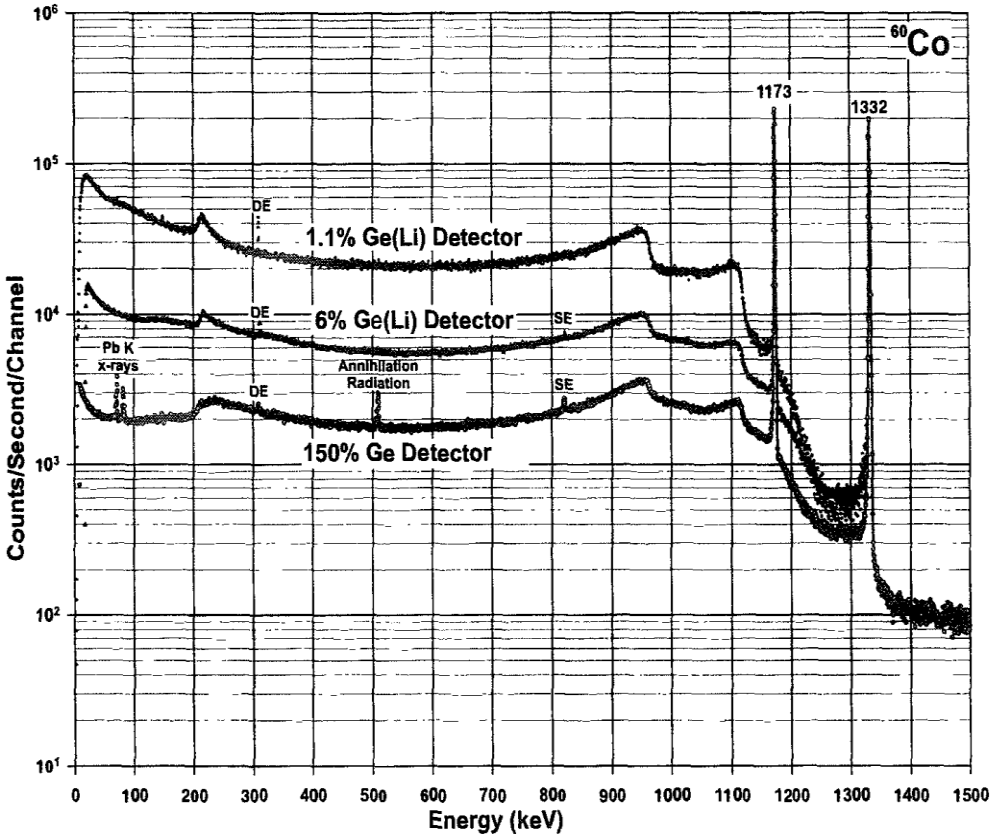

Figure 1.5: ^{60}Co gamma ray spectrum for germanium detectors of three different sizes with the relative efficiencies (see paragraph 1.4.4) shown **[2]**.

1.3.5 Effects on detector performance [2]

Semiconductor detectors are sensitive to performance degradation because of damage created by incident radiation. Radiation damage increases the amount of hole trapping in the active volume of the detector, then it is possible to have a loss in the charge collected. For the HPGe detectors it is found that n-type detectors show less performance degradation from radiation damage than p-type detectors [5]. This can be explained because the damage sites preferentially trap holes than electrons.

HPGe detectors have the advantage, with the respect to the Ge(Li) ones (for more details see [2]), that, if the radiation damage occurs, it can be fixed by annealing the detector. Rising the temperature to 120° for 72 h can restore damaged detectors to their original

features [6]. During this heating process, an external vacuum pump is needed to preserve the cryostat vacuum.

1.4 Gamma spectrometry

1.4.1 Detector response function

Gamma rays can interact with matter in many different ways, but there are three mechanisms really important for radiation measurements: photoelectric effect, Compton scattering and pair production. By these interactions, an incoming photon transfers all or part of the energy to an electron. The photoelectric effect is really relevant for low energy photon (up to many hundreds of keV) and it is highly influenced by the material atomic number, while pair production can only happen for gamma rays with energy higher than 1.02 MeV (2x511 keV). The Compton scattering covers a range of gamma energies between these two extremes. Anyway, the preferred interaction for spectroscopy is photoelectric effect and, for this reason, high atomic number materials are chosen for the detectors. Size, shape and composition of the detector can influence the response function. For example, with a large detector all the radiations are absorbed and the spectrum consists in a single full energy peak. For a small detector, instead, it is possible to see also Compton continuum at low values energy and, if pair production happens, double escape peak. For a real detector we have to consider that Compton scattering can influence the full energy peak and it is possible to see a single escape peak (Figure 1.6).
The spectrum is complicated to predict and the best method to do it is using of Monte Carlo simulations, which simulates the histories each single particles.
Among the properties of the response function, the most important is the photofraction (or intensity), that is the ratio of the area under the photopeak to the area under the entire spectrum. This value is important because it indicates the probability that a gamma ray deposits its full energy within the detector. The higher is the photofraction, the lower is the effect of Compton and double escape peaks.

To complicate the spectrum, secondary radiations can be present, like secondary electron, Bremsstrahlung and X-ray characteristic escape peaks. In addition, the surrounding materials can produce the annihilation peak (511 keV) or backscattered gamma rays [2].

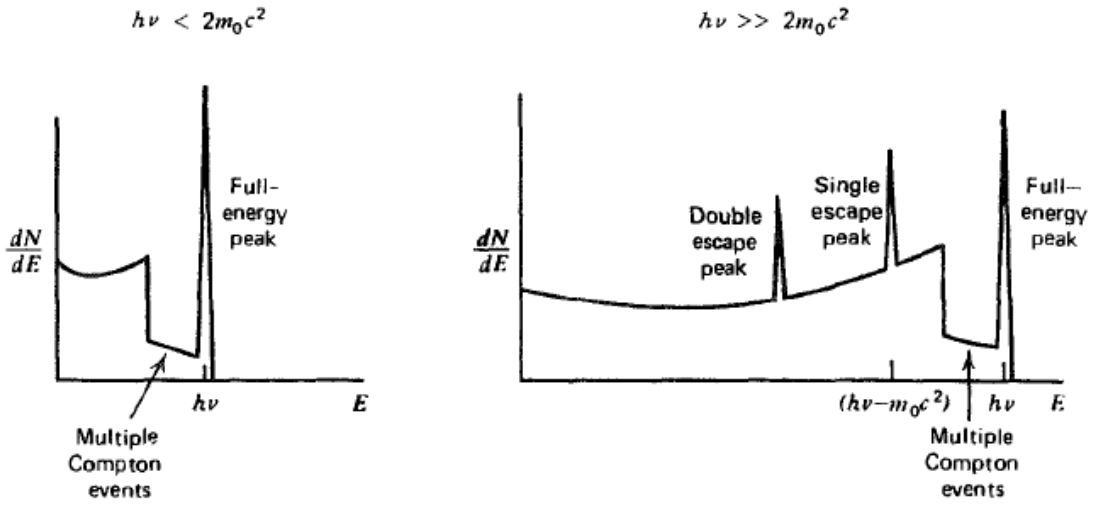

Figure 1.6: intermediate detector size spectrum **[2]**.

1.4.2 Energy calibration

When installing a new spectrometric equipment, different calibrations have to be considered. The energy calibration is necessary to establish the relation between the energy released by the radionuclide and the channel in which this energy is stored. To start, amplification gain of the amplifier is adequately chosen and then it is possible to evaluate more precisely the coefficients of the fitting curve. This curve (Figure 1.7), that is used to calibrate the analog-to-digital conversion range (ADC) in energy level (keV), has the typical formula of

$$E_\gamma[keV] = c_0 + c_1 C(channel) \qquad \text{(Eq. 3)}$$

Where:

c_1 = linear energy scale [slope in keV/channel] of MCA (Multi-Channel Analyser);[1]

c_0 = intercept, very close to zero.

[1] Multi Channel Analyser is a laboratory instrument which can measure distributions of input signals consisting of pulses.

The slope of the calibration curve shows how large the energy range covered by the detector is. Then, taking into account what energies of gamma rays we expect, the energy window is defined. Many measurements with a known source (like ^{152}Eu or ^{241}Am) are done to evaluate c_1 and c_0. In this way, it is possible to find the relation between channel and energy and to know the exact position of a peak of known energy. After the calibration, a source with other gamma ray peaks can be measured to check the obtained energy calibration curve (through the software *Genie2000* from Canberra) [4].

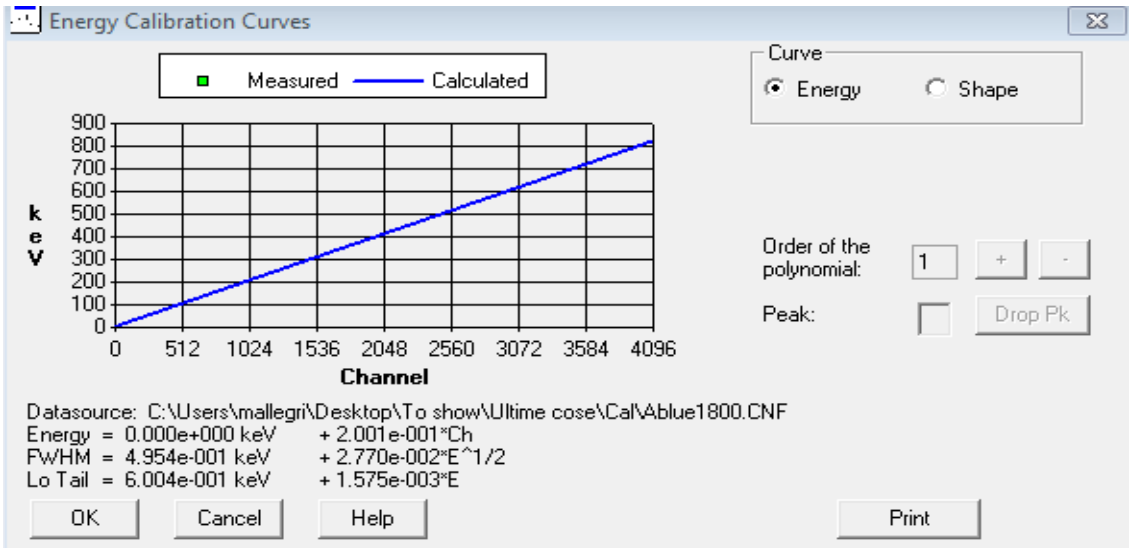

Figure 1.7: energy calibration curve in *Genie 2000 Gamma Spectrometry Software from Canberra*

After establishing this relationship, the coefficients are recorded in the software and they will automatically be used in the next measurements, until a new energy calibration is entered. An energy recalibration is often necessary because the initial conditions are not stable in the time and a shift of the calibration could be observed.

1.4.3 Resolution calibration

The resolution is a parameter that indicates the ability to resolve close peaks in a spectrum. A fundamental parameter that defines resolution is the Full Width at Half Maximum (FWHM) (Figure 1.8).

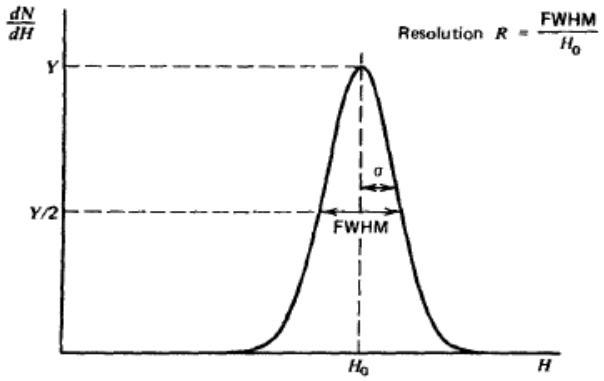

Figure 1.9: definition of detector resolution **[2]**

This formula has the assumptions that background or continuum, on which the peak is superimposed, is negligible or has been subtracted [2]. FWHM is an indication of the width of the peak; if its value is small, the peak will have a narrow shape and it will be easier to discriminate different peaks with energies close one to each other. FWHM is expressed in keV, if we consider its absolute value, or it can be expressed relatively to the corresponding energy. It is dependent from the energy, it increases when energy increases, but it is also dependent from the detector properties, especially detector type (NaI, Ge or LaBr) (Figure 1.9).

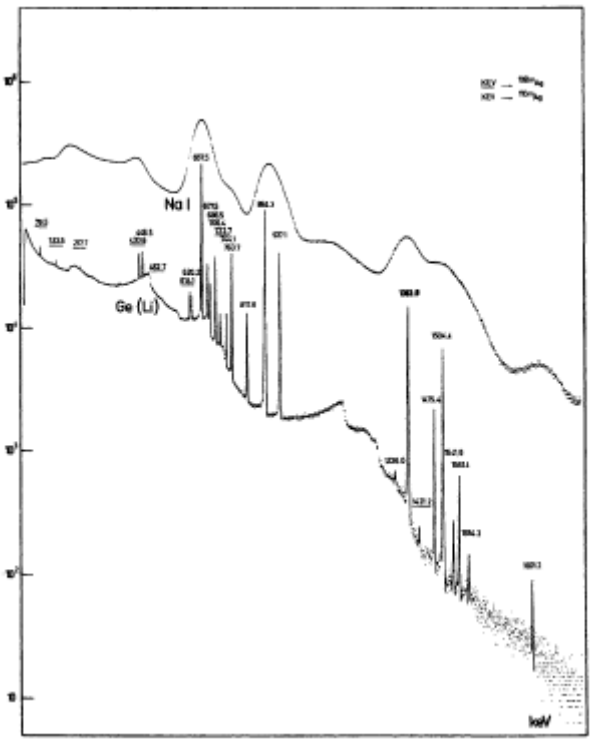

Figure 1.8: comparative pulse height spectra recorded using sodium iodine scintillator and Ge(Li) detector. **[2]**

With an appropriate calibration with a known source, the software (in this case *Genie 2000 Gamma Spectrometry* from Canberra), can find a mathematical relation between energy and FWHM and create a fitting curve (Figure 1.10). The formula used is

$$\mathrm{FWHM[keV]} = \mathrm{F_0} + \mathrm{F_1}\ \sqrt{E} \qquad \text{(Eq. 4)}$$

Where *E* is the energy of the gamma ray.

After finding this curve, it is possible to know the expected FWHM for an energy of interest. This will help in the detection of small peaks in a spectrum and to identify if a raise in counts is related to a peak (Gaussian with FWHM equal to calibration value) or if it is noise.

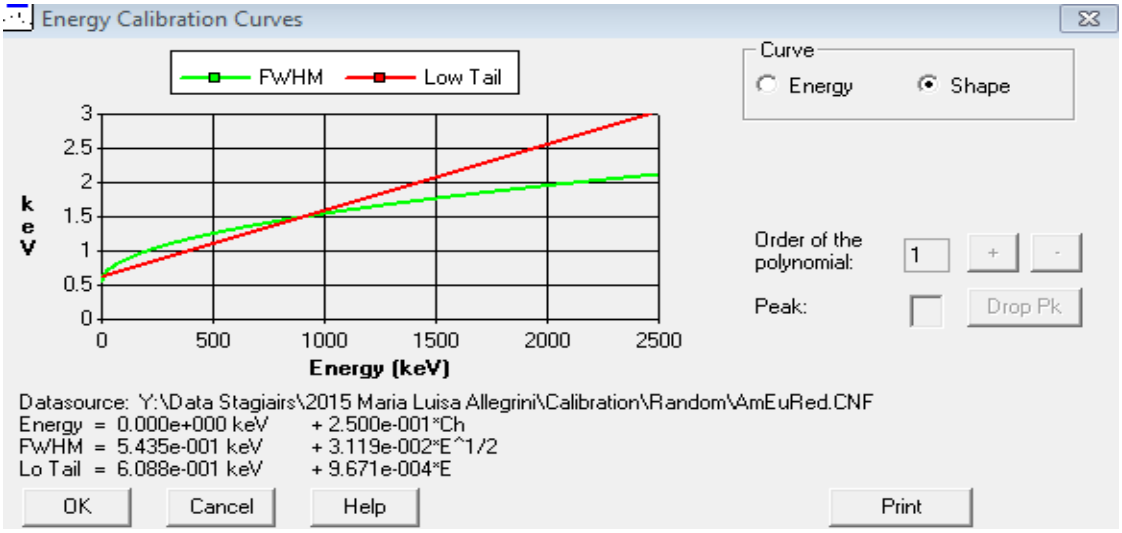

Figure 1.10: resolution calibration from Genie 2000 Gamma Spectrometry Software from Canberra

1.4.4 Efficiency calibration

Uncharged radiations, like gamma rays, often undergo many interactions before arriving to the detector and being detected. The detection efficiency for this type of radiations is always less than 100%, while for charged particles (as α and β) it can reach 100%.

It is possible to subdivide the counting efficiency in different classes:

- Absolute efficiency: $\varepsilon_{abs} = \dfrac{\text{number of pulses recorded}}{\text{number of radiations emitted by source}}$

- Intrinsic efficiency : $\varepsilon_{int} = \frac{\text{number of pulses recorded}}{\text{number of radiations incident on detector}}$
- Relative efficiency: $\varepsilon_{rel}\ (1332\ \text{keV}) = \frac{\varepsilon_{\text{abs}}}{\varepsilon_{3"\text{x}\,3"\ \text{NaI(Tl)}}(1332\ \text{keV})}$

In the next, when referring to efficiency, what is meant is the absolute efficiency. Efficiency is not only dependent on the detector, but also from geometry, size and density of the sample, and its distance from the detector. A specific efficiency calibration is then necessary for all the different measurement setup. To evaluate the counting efficiency, a certified source sample, with uncertainty and assay date is used. To cover the energies of interest, a calibration source, which includes radionuclides emitting a broad range of gamma ray energies, is needed to calculate the detection efficiency, as a function of gamma ray energy (keV). For each considered gamma line, a peak is fitted which gives us the net count of the peak. The activity of the source, the intensity of the gamma ray line of that specific radionuclide and the measurement time are then taken into account to calculate the efficiency.

$$\varepsilon = \frac{N\ [counts]}{A\ [Bq] * I_{\gamma}\ * t[seconds]} \qquad \text{(Eq. 5)}$$

Where:

N = number of counts (net peak area);

A= source activity (constant value during the measurements, with the respect to nuclide's half-life);

*I*γ= emission probability (or intensity), that is the fraction of disintegrations that result in the emission of a photon at a certain energy;

t = time of the measurement.

These calibration samples must satisfy many characteristics, like having a similar geometry to the subject that has to be analysed, containing radionuclides that cover the energy range needed for the measurements, being well certified and robust.

The software to create a fitted curve (Figure 1.11) can use efficiency data at different energies.

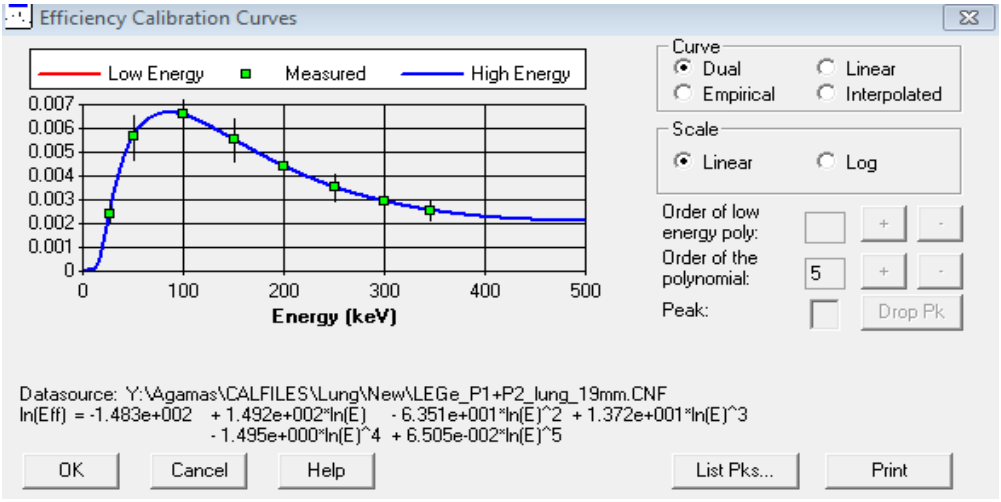

Figure 1.11: efficiency calibration curve from *Genie 2000 Gamma Spectrometry Software from Canberra*

The strong energy dependence of the total detection efficiency causes the recorded photon intensities to be significantly different from the emitted intensities. To perform quantitative assays involving comparison of the intensities of different gamma rays, one must take into account this energy-dependent efficiency correction.

When low-energy gamma-ray assays are performed, thin detector volumes should be used. This optimizes the detection efficiency in the low-energy region and reduces the detection efficiency for the unwanted high-energy gamma rays.

When high-energy gamma-ray assays are performed, thick detector volumes should be used to provide adequate efficiency for the more penetrating radiation. In addition, selected absorbers at the detector entrance can reduce contributions to the counting rate from unwanted low-energy radiation.

When efficiency coefficients and the curve are found, it is possible to calculate the activity of an unknown source, through the inverse formula considering one of the full energy peaks present in the spectrum:

$$A\,[Bq] = \frac{N\,[counts]}{\varepsilon\, I_\gamma\, t[seconds]} \qquad \text{(Eq. 6)}$$

2 ANTHROPOGAMMAMETRY

2.1 General features

Anthropogammametry (AGM) is the direct measurement of internal contaminations in the human body. Internal contamination occurs when people swallow or breathe in radioactive materials, or when radioactive materials enter the body through an open wound or are absorbed through the skin. A fraction of radioactive materials stays in the body and is deposited in different organs, while the other is eliminated from the body in blood, sweat, urine, and feces. AGM uses the technique of gamma ray spectrometry to assess the radioactivity inside the body. The result of a measurement is a gamma-spectrum. Analysing the peaks in the spectrum permits identification and quantification of the nuclides present in the body. The photon energy, at which a peak appears in the spectrum, is radionuclide specific and its activity is proportional to the area of the detected peak.

2.2 In-vivo monitoring

Direct measurements of body or organ give a quick estimate of the activity, but this is possible only for radionuclides emitting radiations that can be detected outside the body. Facilities for the measurement of the body consist in high efficiency detectors housed in well-shielded, low background environments. These detectors must have a geometrical configuration that suit with the purpose of the measurements. In special or unusual investigations it may be better to determinate the distribution of the activity with a scan of the whole body or to analyse the relative response of the detector at different positions. This technique can be used for radionuclides that emit:

• γ or X rays; as example ^{235}U and ^{241}Am t can be detected by their characteristic 186 and 59 keV γ rays or ^{238}Pu can be detected by its 13, 17 and 20 keV X-rays.

• Positrons (from annihilation photons);

• Energetic β particles;

To monitor radionuclides with the accuracy required for radiation protection purpose (with very low activities), instead, high sensitivity techniques are needed. If we consider Pu isotopes, which emit only very low intensity gamma rays, it is not possible to detect

their x-rays in radiation protection, unless ^{241}Am is present. Many facilities used tallium activated sodium detectors, which present the advantages of having big crystal and high detection efficiency for γ rays (for whole body counting). Now high-efficiency germanium detectors are preferred when workers are exposed to unknown γ ray emitters. These detectors have a high energy resolving power and this makes analysing the resulting spectra easier, but a proper calibration is still needed. Most laboratories use a physical phantom, like BOMAB (Bottle-Manikin-Absorption) phantom for Whole Body Counting (homogeneous distribution of activity in complete body) or a Lawrence Livermore thorax phantom with radioactive organs for the calibration activity, but there are many limitations with respect to the body size, body shape and radionuclide distribution. It is also possible to use numerical calibration techniques or mathematical voxel phantom and Monte Carlo simulations.

2.3 Internal dosimetry

To introduce AGM in a broader context, it intends to estimate the activity retained in the body, but that positive values should then be interpreted to internal doses.
The evaluation process for internal doses can be divided in two phases:

- determination of the amount of radioactive material in the human body, using direct or indirect measurements methods;
- Interpretation of the intake and internal dose, considering several influencing factors and assumptions, about biokinetic and energy absorption processes.

The principal routes of entry into the body are the respiratory tract, the gastrointestinal tract and the skin (intact and wounds). Some activity is also absorbed into blood and body fluids. Then it withstands many transfers and it can distribute in the body or it also can be eliminated. The distribution of the activity can be homogeneous (with tritiated water) or localised in specific organ or tissues (iodine for the thyroid and plutonium for lungs and liver). Elimination of the activity, instead, can happen by urinary and faecal excretion (Figure 2.1).

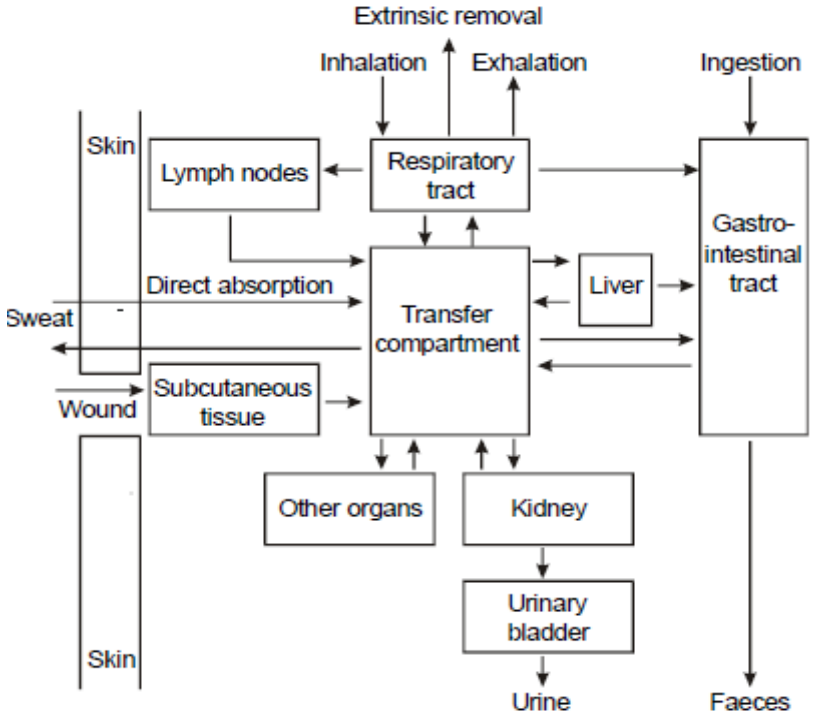

Figure 2.1: main routes in intake, transfers and excretion of radionuclides in the body **[8]**

Beyond intake via ingestions or inhalation, it is also necessary to consider direct uptake from contamination of the skin. The only case considered by the ICRP is tritiated water, but absorption trough skin is not included in the derivation of the dose coefficient for this radioactive substance. In addition, iodine can be taken up through the skin, but to a lesser extent [7].

2.3.1 Human respiratory tract model

In the model described in the ICRP Publication 66 [8], the respiratory tract is divided in 5 regions (Figure 2.2):

- Extra thoracic tract (ET) airways, divided into anterior nasal passage (ET_1) and pharynx and larynx (ET_2);
- Thoracic tract, divided into bronchial region (BB) that consists in trachea and bronchi, bronchiolar region (bb) and alveolar-interstitial region (Al).

Lymphatic tissue is associated to the extra thoracic and thoracic regions (LN_{ET} and LN_{TH}).

This model can be applied for workers and the public for inhalation of particles, gases and vapours. The "reference worker" for inhalation is a male breathing normally through the nose while performing light work.

The main processes taken into account are particles deposition and clearance.

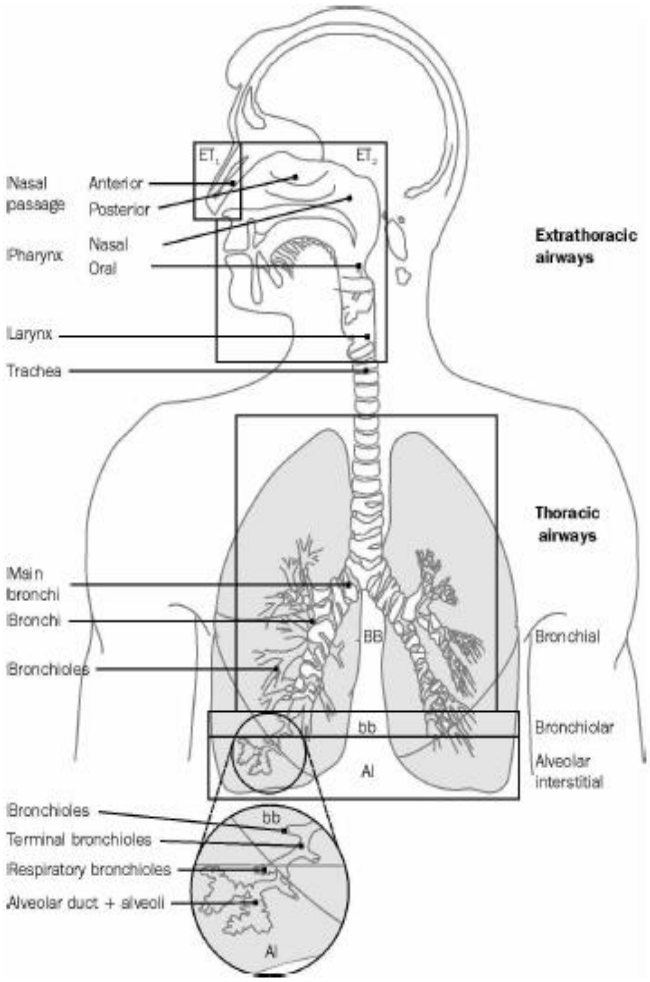

Figure 2.2: human respiratory tract **[8]**

The first one considers the deposition in each region, for the size of interest (0.6 nm – 100 µm). The regions are considered as a series of filters during inhalation and exhalation and the efficiency is calculated with thermodynamic and aerodynamic processes. Deposition parameters are evaluated for three different categories of exertion of work: sitting, light and heavy work.

For the occupational exposure the recommended default value for the Activity Median Aerodynamic diameter (AMAD) is 5 µm. Fractional deposition in each region is given in Table1.

Table 1: Regional deposition of inhaled 5µm AMAD in Reference Worker **[8]**

Region	Deposition (% of inhaled activity)
ET_1	34.0
ET_2	40.0
BB	1.8
Bb	1.1
Al	5.3
Total	82.0

Clearance from the respiratory tract is the other main process. Material deposited in ET_1 region is removed also with a simple nose blowing. In the other regions, clearance is competitive with particle movements to the Gastro-intestinal (GI) tract and lymph nodes and the absorption of material into blood (Figure 2.3). The particle transport rates are assumed the same for all the materials. The absorption is divided in two steps: dissociation of the particles into material that can be absorbed into bloody fluids, and absorption into body fluids of soluble material and of material dissociated from particles (uptake). Anyway, there is a simultaneous absorption into the blood, in general.

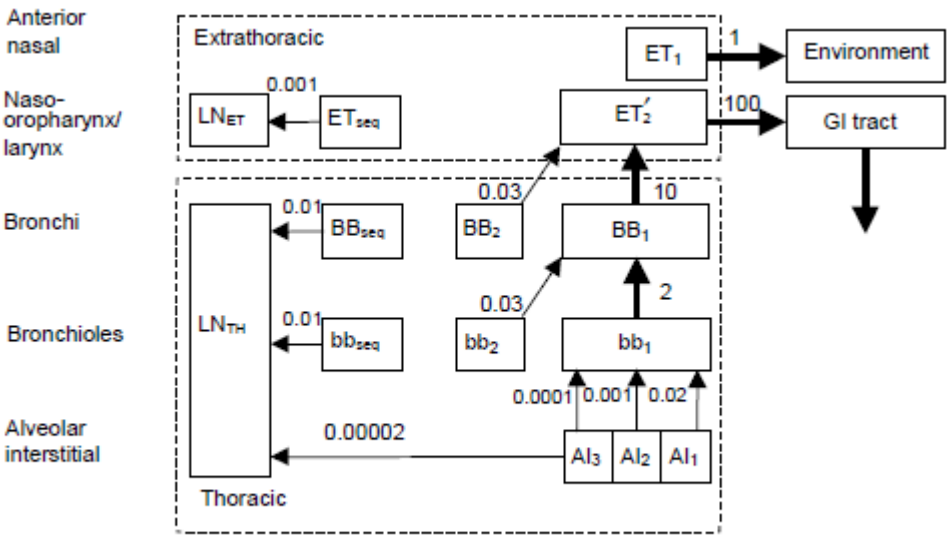

Figure 2.3: compartment model representing particle transport from each respiratory tract region Values alongside the arrows represent the fraction retained in the various parts **[8]**.

3 SCK-CEN ANTHROPOGAMMAMETRY LABORATORY

3.1 General features

In the SCK-CEN Anthropogammametry Laboratory (located in Belgium), workers from nuclear facilities (belonging to SCK-CEN and other companies) are screened for internal contamination, because they can inhale or swallow radioactive material. Every year more than 1000 measurements are carried out. The biggest advantage of this kind of laboratory is to have the capability of directly measuring the internal contamination with a fast response (less than one hour), but some nuclides have very high detection limits so it is not possible to detect them. On the other side, times of calibration could be long and it is not always convenient to do the measurements outside the bunker (also if there are some portable equipment that can be used outside).It also has to be considered that there are many geometry uncertainties, because we are dealing with people.

3.2 Preparation to the the measurements

Before each measurement it is necessary assure that people have no external contaminations. For this reason first they have to screen hands and feet in a α and β counter (Figure 3.1).

Figure 3.1: counter for external contamination (hands and feet)

Then they have to take a shower and wear a "jogging", provided by the laboratory staff. The reasons of taking a shower and changing the clothes is to avoid any contamination of the measurement room because, if this happens, a wrong evaluation of the retained activity could be done. After that, the worker is ready to be screened in one of the two bunkers settled up for the measurements.

3.3 Bunker structure

Routine measurements are located in shielded rooms, which have a background radiation 100 times less than the natural one. This is done to avoid noise in the spectrum, which increases the minimum detectable activities, a very important aspect, since we are looking for very small activities within the human body. The structure of the bunker walls are made of suitable materials to reduce background radiation and to absorb the scattered photons emitted by the person. The walls, ceiling and floor are made of (from the outside to the inside):

- 20 cm of steel (90 tons weight) to reduce background radiation ;
- 3.2 mm of lead to absorb secondary radiation;
- 1 mm of Sn (tin);
- 0.5 mm of Fe (iron).

The materials atomic number decreases from the extern to the intern to absorb low and lower gamma rays energies.
Lead and the steel are selected with a very low amount of natural activity, indeed steel often contains traces of ^{60}Co, ^{40}K, ^{226}Ra. The lead is coming from sunken ship that laid on the bottom of the ocean during WWII (Figure 3.2).

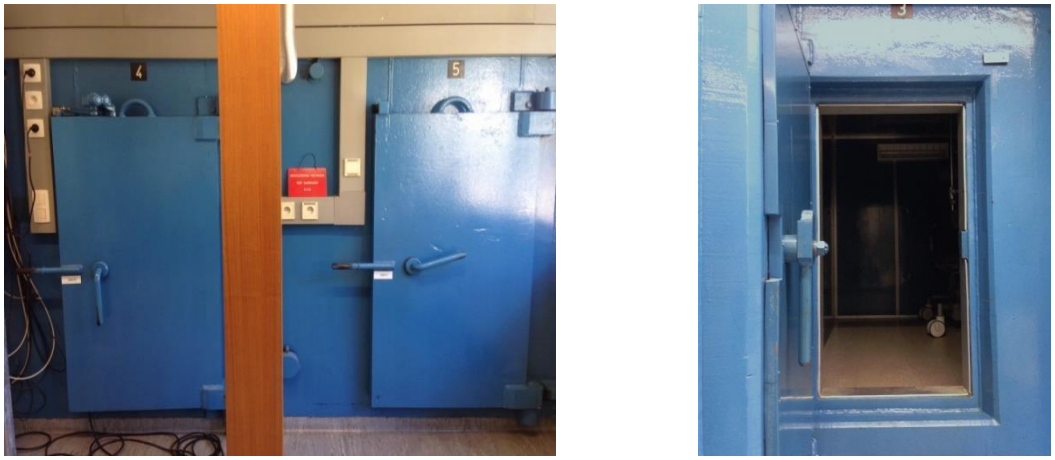

Figure 3.2: bunker overview

Two main types of monitoring are routinely done: whole body counting and lung measurements.

3.4 Whole body counting

For Whole Body Counting (WBC), the equipment is a large scintillation detector (NaI). Because this detector has a high volume, it has a high efficiency, which allows detecting low activities of gamma emitters in the body (Figure 3.3).

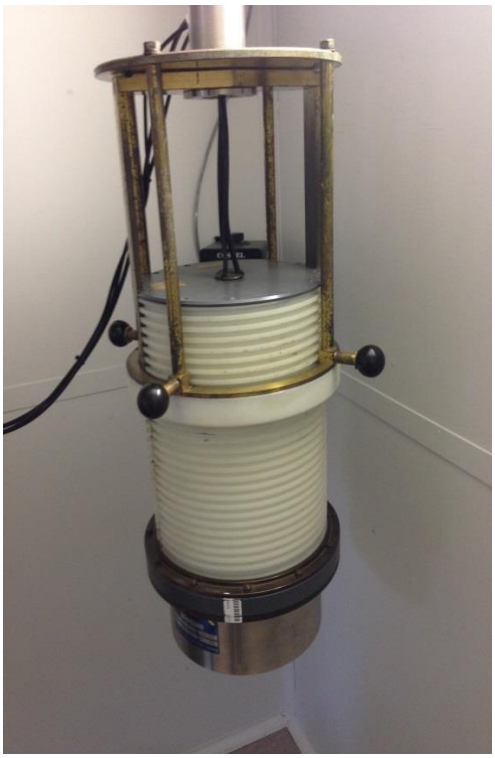

Figure 3.3: NaI detector for whole Body Counting

This screening is usually done to investigate the presence of fission products (^{137}Cs, ^{131}I, ^{90}Sr) or activation products (^{60}Co, ^{41}Ar, ^{90}Y). Through a measurement of 30 minutes, ^{60}Co and ^{137}Cs can be detected, with a detection limit of about 25 Bq. ^{40}K is always found in the body with an activity of 3000 to 6000 Bq. NaI detectors have a bad resolution compared with semiconductor detectors, so calibration is done with different nuclides not at the same time with a modular phantom with interchangeable sources. The phantoms are made out of material with a density close to the mean density of the human body with holes to enter the calibration sources.

In this laboratory, there is also equipment for thyroid screening. When an iodine contamination is suspected, measurements of thyroid will be done putting the detector

(for example BEGe (Berylliums Germanium) shown in Figure 3.4) close to the neck. This is not done routinely, only when direct measurements are needed to evaluate the received dose, since iodine has a half time of about 8 days.

Figure 3.4: BEGe detector for thyroid monitoring

3.5 Actual setup for lung monitoring

The goal of lung monitoring is to detect if the person has inhaled a radionuclide, as 239Pu. People working with plutonium or uranium are the candidates for these measurements. Plutonium isotopes emit gamma rays only with very low intensities, so a daughter nuclide, ^{241}Am, has to be analysed. The ratio Pu/Am is an important value to know in this case. Americium emits a low energy gamma ray of 59 keV and, for this reason, Low Energy Germanium detectors (LEGe) are used (Figure 3.5).

These detectors have worse efficiency than scintillators due to their smaller size, but their resolution is better. This setup, active now, is made up of two LEGe detectors pointing on the right lung (which is bigger than the left one, because of the heart). A routine measurement takes 50 minutes and the detection limit for ^{241}Am is between 6 and 18 Bq. Since we are dealing with low energy gamma rays, absorption in overlaying tissues plays an important role.

Figure 3.5: LEGe detectors for lung monitoring

For this reason a phantom with tissue equivalent overlay plates is used for calibration and different overlay thicknesses are needed to cover the range of chest walls usually encountered. To estimate the chest wall thickness of a person coming for a routine measurement, a formula is used, which takes into account length, weight and age of the person [9]:

$$\mathrm{CWT} = -0.1 + \frac{0.133 * w}{(h)^2} - 0.004 * a \qquad \text{(Eq. 7)}$$

Where:

CWT = chest wall thickness (cm)

w = weight (kg);

h = height (m);

a= age (years)

3.6 New setup for lung monitoring

Recently three new HPGe detectors have been purchased to replace the setup using LEGe detectors (Figure 3.6). The goal is to achieve a better efficiency than what can be obtained with the previous setup. This is expected for two reasons:

- Detector volumes are bigger compared to LEGe's;
- One extra detector increases the efficiency (Two for the right lung and one for the left one).

These new detectors are placed in another bunker with a new chair, intended for medical purpose, which is expected to be more comfortable than the previous one, since the lung monitoring is a long measurement.

In order to function properly, the new High Purity Germanium detectors (HPGe) must be cooled to a temperature of 85-105 K. These low temperatures allow the crystal to operate as a diode, to produce a current proportional to the energy deposited by gamma rays. To reach this temperature liquid nitrogen (LN_2) is mostly used, but in our case, electrical coolers have been chosen. Electrical coolers have less safety hazards than LN_2 and they provide cooling as long as electricity is available. The cooler includes a compressor which acts on a special gas mixture (cooling), a transfer hose, a heat exchanger and a cold head. The transfer hose contains the gas pressure and the return lines and is made of stainless steel. At one of its ends, there is the heat exchanger, a coiled set of copper and stainless tubing mounted inside a stainless tube. In this part, the gas expansion for the necessary cooling takes place [10].

Figure 3.6: ORTEC detector for lung monitoring

Here we can see the data sheet of one of the three detectors (Figure 3.8), called Blue. To differentiate them one from each other, it has been decided to give them names, which are Blue, Green and Red. They work at different voltages, respectively 3400, 4000 and 2300 Volts.

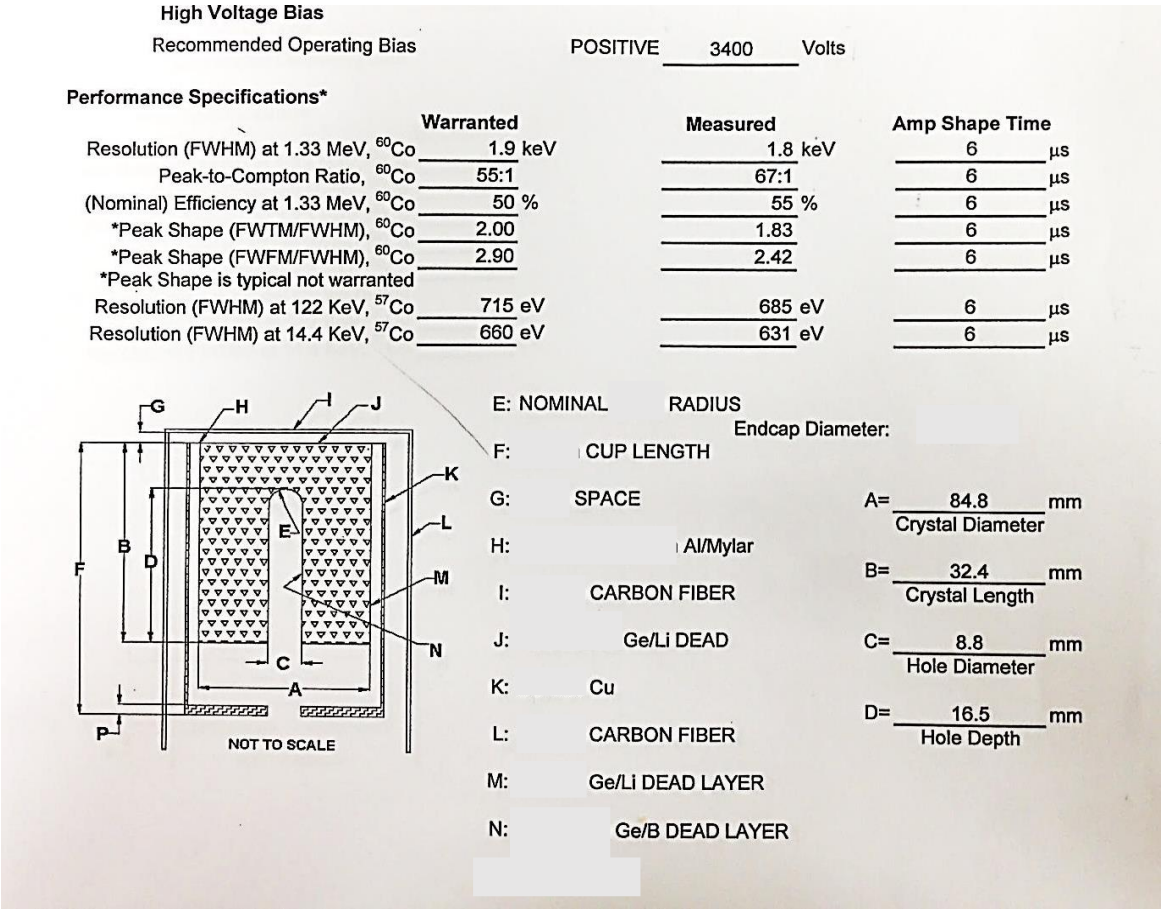

High Voltage Bias

Recommended Operating Bias — POSITIVE 3400 Volts

Performance Specifications*

	Warranted	Measured	Amp Shape Time
Resolution (FWHM) at 1.33 MeV, ^{60}Co	1.9 keV	1.8 keV	6 µs
Peak-to-Compton Ratio, ^{60}Co	55:1	67:1	6 µs
(Nominal) Efficiency at 1.33 MeV, ^{60}Co	50 %	55 %	6 µs
*Peak Shape (FWTM/FWHM), ^{60}Co	2.00	1.83	6 µs
*Peak Shape (FWFM/FWHM), ^{60}Co	2.90	2.42	6 µs
*Peak Shape is typical not warranted			
Resolution (FWHM) at 122 KeV, ^{57}Co	715 eV	685 eV	6 µs
Resolution (FWHM) at 14.4 KeV, ^{57}Co	660 eV	631 eV	6 µs

E: NOMINAL RADIUS
Endcap Diameter:
F: CUP LENGTH
G: SPACE
H: Al/Mylar
I: CARBON FIBER
J: Ge/Li DEAD
K: Cu
L: CARBON FIBER
M: Ge/Li DEAD LAYER
N: Ge/B DEAD LAYER

A= 84.8 mm — Crystal Diameter
B= 32.4 mm — Crystal Length
C= 8.8 mm — Hole Diameter
D= 16.5 mm — Hole Depth

Figure 3.8: Data Sheet for "BLUE" ORTEC detector

4 GAMMA SPECTROMETRY FOR LUNG MONITORING

4.1 Introduction

In-vivo monitoring of radiation workers at SCK-CEN has started since the 1960s with different detector systems used during the time. At the beginning, two dual crystal scintillators detectors (Phoswich type) composed the setup for routine lung monitoring; then they were replaced with a high-resolution low energy germanium detector array. Since 1994 these low energy HPGe detector system with few detector, but larger than the previous ones, has been used for monitoring.
Two setups, with different number of channels and energy range, have been settled:

- 4k: low-medium energy range (10-810 keV) with 4000 channels and 0.2 keV per channel,
- 8k: high energy range (25-2048 keV) with 8000 channels and 0.25 keV per channel;

For the second one only energy calibration and quality assurance have been performed, because it is not intended for lung measurement. Indeed, it could be used for other measurements, as thyroid, skull and even whole body counting, which is not part of the objectives of this thesis work.
In this work the energy and resolution calibration of all three new HPGe detectors have been established. The efficiency calibration was done using just two out of the three detectors, because one of them (the "Green" one) was damaged by a vacuum lost and was thus not available during the internship.

4.2 Background measurements

The background radiation was measured by collecting a 60000 s spectrum with only the detectors and the chair inside the bunker. The total background, then, was calculated summing the three single spectra.
The same thing was done for the background with the phantom inside. The phantom, with no radioactive lungs, was put on the chair and the detectors in front of it.
In Figure 4.1 and 4.2, it is possible to see the differences between the two spectra. In the low range energy spectra, obviously, it is not possible to see the peak of ^{40}K at 1460 keV, as in the other setup. At low energy, until 77 keV, all the peaks come from X-rays

characteristic of lead, which surrounds the bunker. The other peaks belong to radionuclides of one of the three natural chains of decay, in particular of U-238 (186 and 609 keV) and Th-232 (238 and 583 keV).

Also for the high-energy range, we have the same results and the majority of the peaks come from the chains of U-238 and Th-232.

Anyway these peaks are very small and this is because the materials and the thickness of the bunker. Net peak areas reach about 1400 counts in 60000 s (i.e. less than 0.03 counts per second) for the peak with highest intensity (except 511 keV), but not more than that (Table 2).

Table 2: List of background peaks

Energy (keV)	FWHM (keV)	Net Peak Area	Net Area Uncert.	Radionuclide	Decay chain
74.9	0.77	588	38.49	Pb-X	
77.14	0.78	415	35.8	Pb-X	
84.7	0.94	266	35.04	Pb-X	
87.45	0.98	224	34.34	Th-234	U-238
92.85	0.98	320	37.77	Th-234	U-238
186.17	0.84	478	40.33	U-238	U-238
238.98	0.99	1409	48.4	Pb-212	Th-232
242.28	0.99	265	32.28	Pb-212	Th-232
295.56	0.96	550	36.2	Pb-214	U-238
300.43	0.96	108	26.81	Th-232	Th-232
338.42	0.69	119	26.98	U-238	U-238
352.23	1.15	993	40.07	Pb-214	U-238
511.19	2.36	4009	60.92	Annihilation	
583.28	1.25	587	29.37	Tl-208	Th-232
609.34	1.21	814	33.69	Bi-214	U-238
661.7	1.16	133	19.41	Cs-137	
727.46	1.21	114	18.05	Th-232	Th-232
768.46	0.44	48	11.78	Bi-214	U-238
846.77	1.08	142	18.68	Bi-214	U-238
860.41	0.6	45	11.96	Th-232	Th-232
911.08	1.59	232	19.71	Th-232	Th-232
933.97	1.5	49	49	Th-232	Th-232
964.51	1.03	47	11.85	Th-232	Th-232
968.86	1.04	110	15.35	Th-232	Th-232
1000.81	1.71	53	13.39	U-238	U-238
1120.15	1.71	184	18	Bi-214	U-238
1238.06	2.04	115	16.1	U-238	U-238
1460.37	1.99	564	25.61	K-40	
1763.84	2.14	124	14.69	U-238	U-238

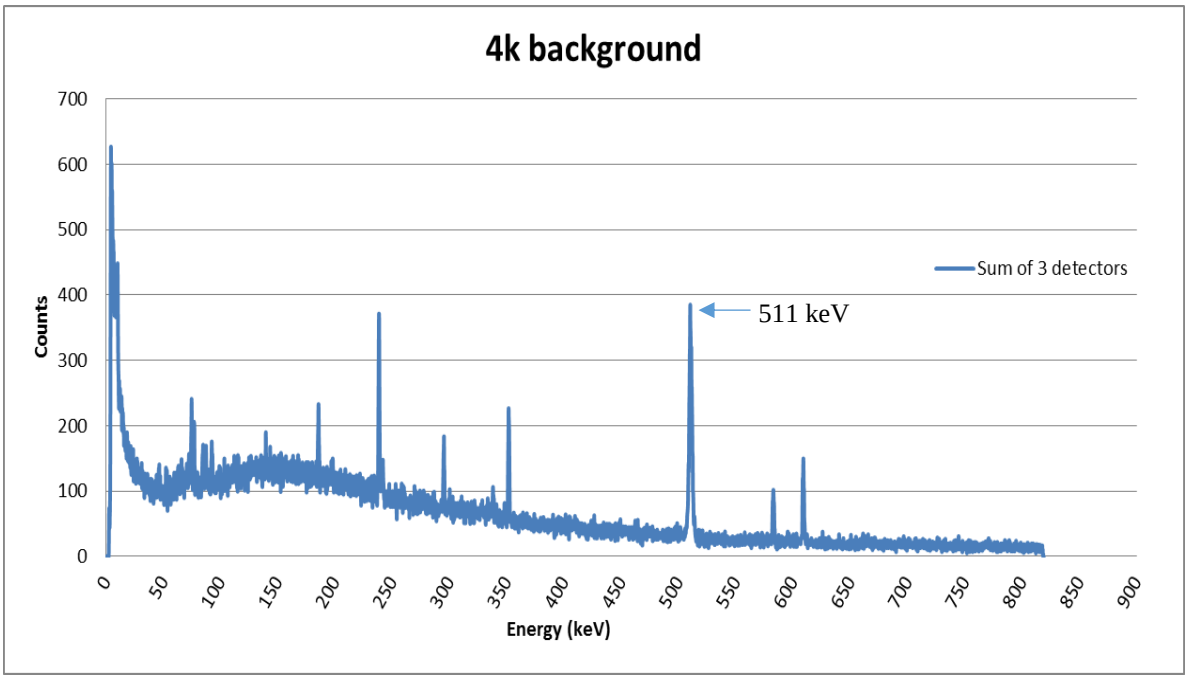

Figure 4.1: background spectra for 4K setup (Sum of three)

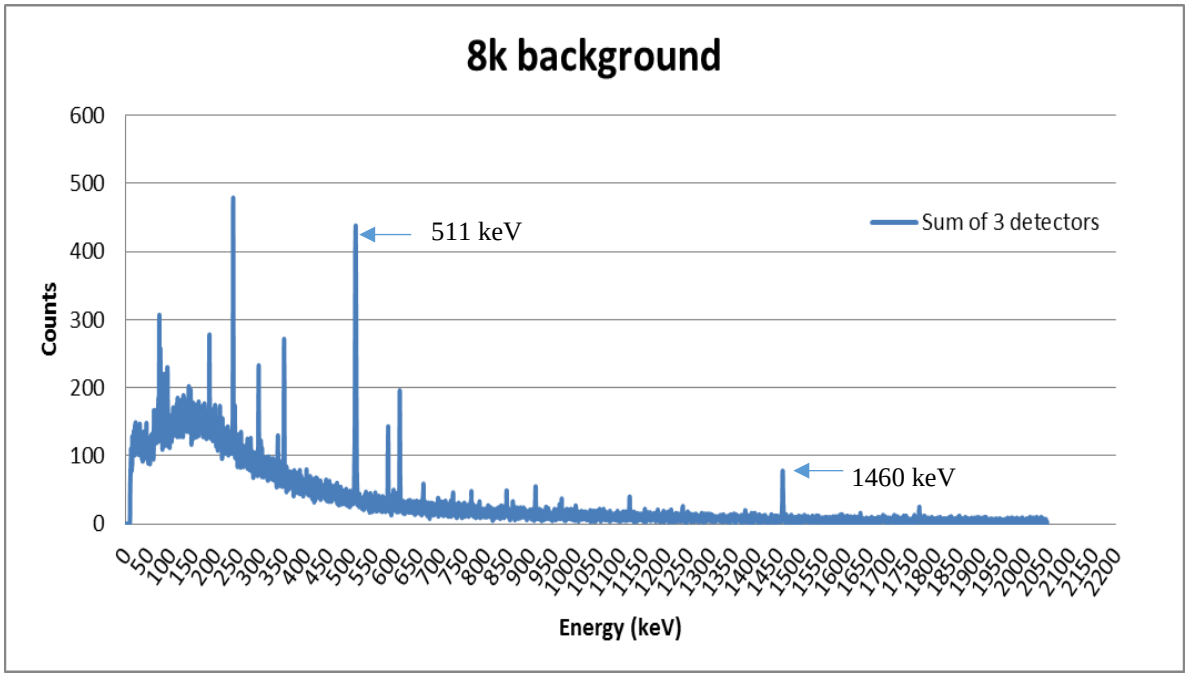

Figure 4.2: background spectra for 8k setup (Sum of three)

4.3 Energy and Resolution Calibration

4.3.1 Sources

For energy and resolution (FWHM depending on energy) calibration ^{152}Eu and ^{241}Am sources have been used. In the Table 3 main features are shown. Europium (half-life13.522 years [11]) was used because it has peaks with high intensity as well at low as at high energy, while americium (half-life 432.6 years [11]) covers only low energy range, but it is fundamental for the purpose of these detectors. Table 4 gives an overview of the peaks used for the calibration.

Table 3: calibration sources for energy calibration

	^{152}Eu (1stsource)	**^{152}Eu (2nd source)**	**^{241}Am**
Reference activity (kBq)	74.4 ±1 (2013-01-01)	30.1±0.4 (2013-01-01)	41±4.4 (2009-09-11)
Actual activity (2016-03-07) (kBq)	62.72	25.37	40.58

Table 4: peaks used for calibration

Energy Peak (keV)	**Setup**	**Source**	**Intensity (%)**
26.34	4k	^{241}Am	2.31
59.54	both	^{241}Am	35.92
121.78	4k	^{152}Eu	28.41
344.28	both	^{152}Eu	26.59
778.9	both	^{152}Eu	12.97
1408.01	8k	^{152}Eu	20.85

4.3.2 Results for 4k channels

Measurements of 5000 seconds were performed to evaluate the calibration curve (Figure from 4.3 to 4.14). After that, the peaks of interest were analysed and the coefficients of the calibration curves were optimised using MS Excel. Once the coefficients were found, they were inserted in *Genie 2000* and so the calibration formula was recorded in the detectors. The resolution curve permits to predict the FWHM at every energy.

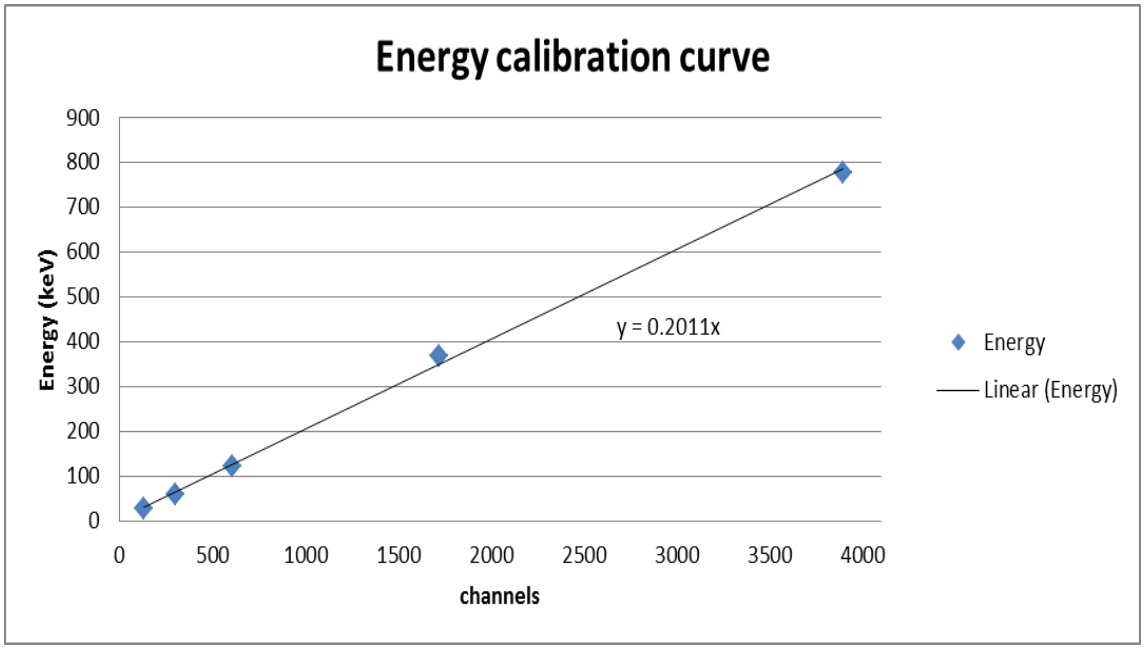

Figure 4.3: blue detector energy calibration curve (4k setup)

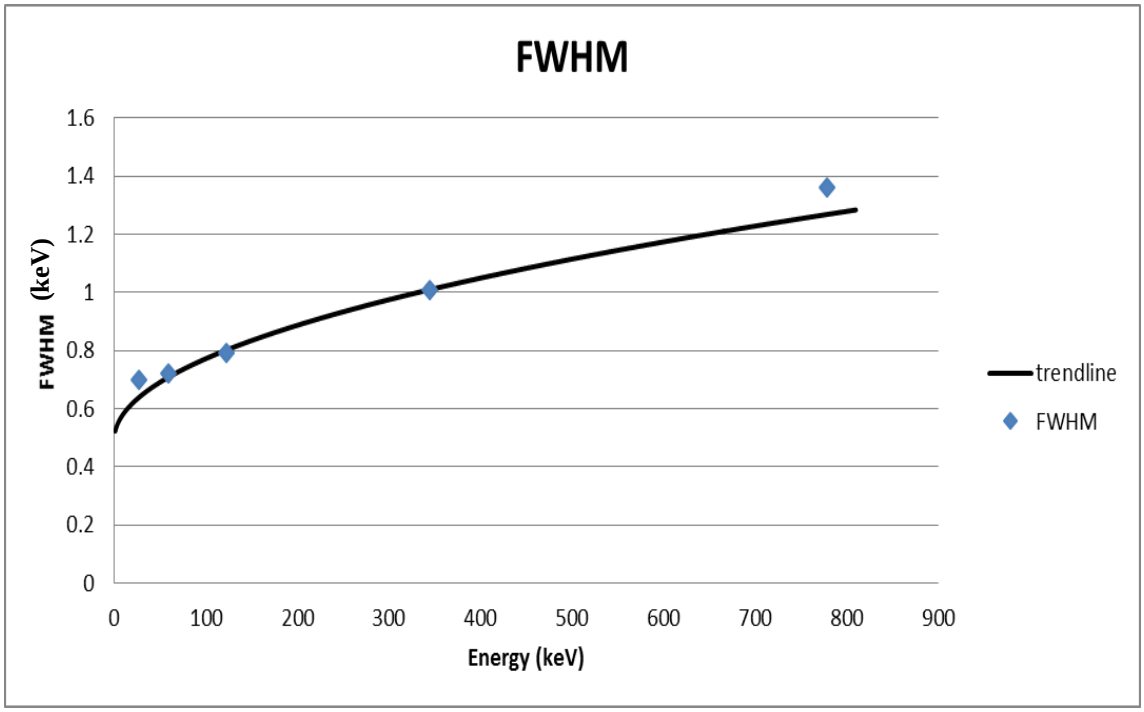

Figure 4.4: blue detector FWHM curve (4k setup)

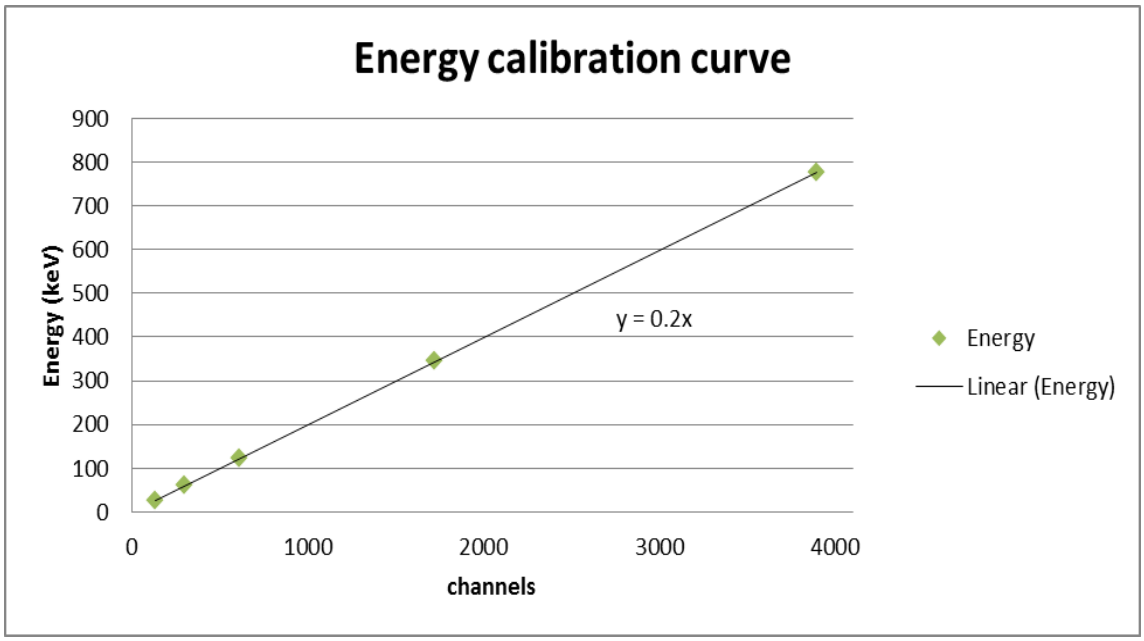

Figure 4.5: green detector energy calibration curve (4k setup)

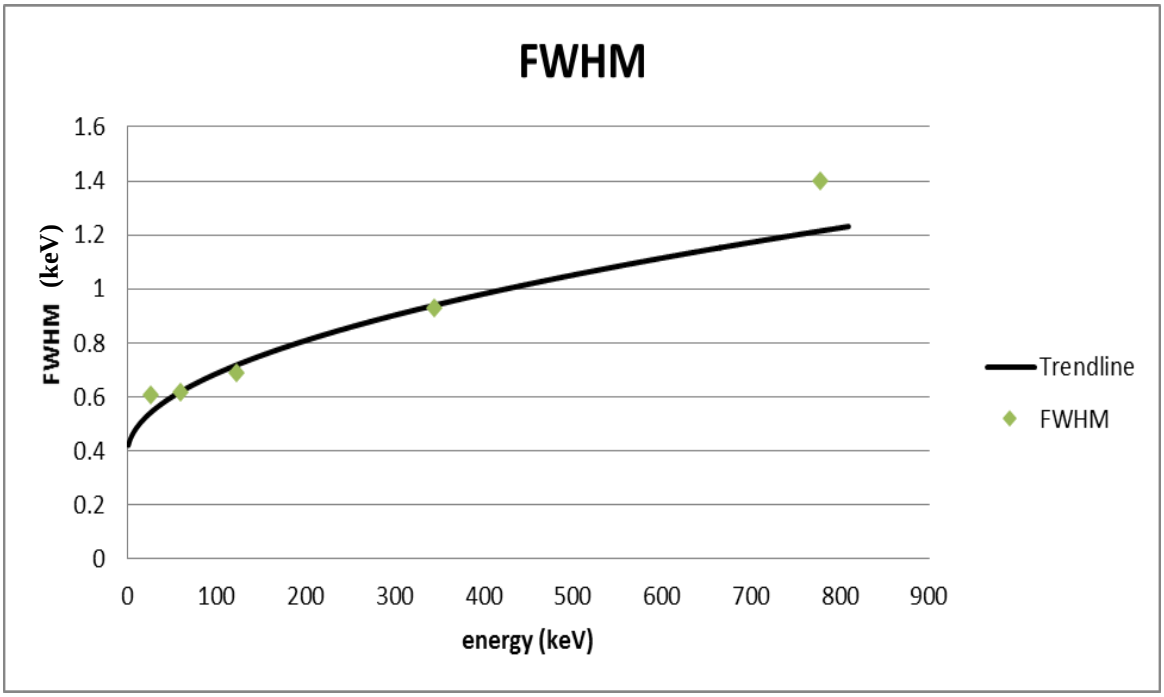

Figure 4.6: green detector FWHM curve (4k setup)

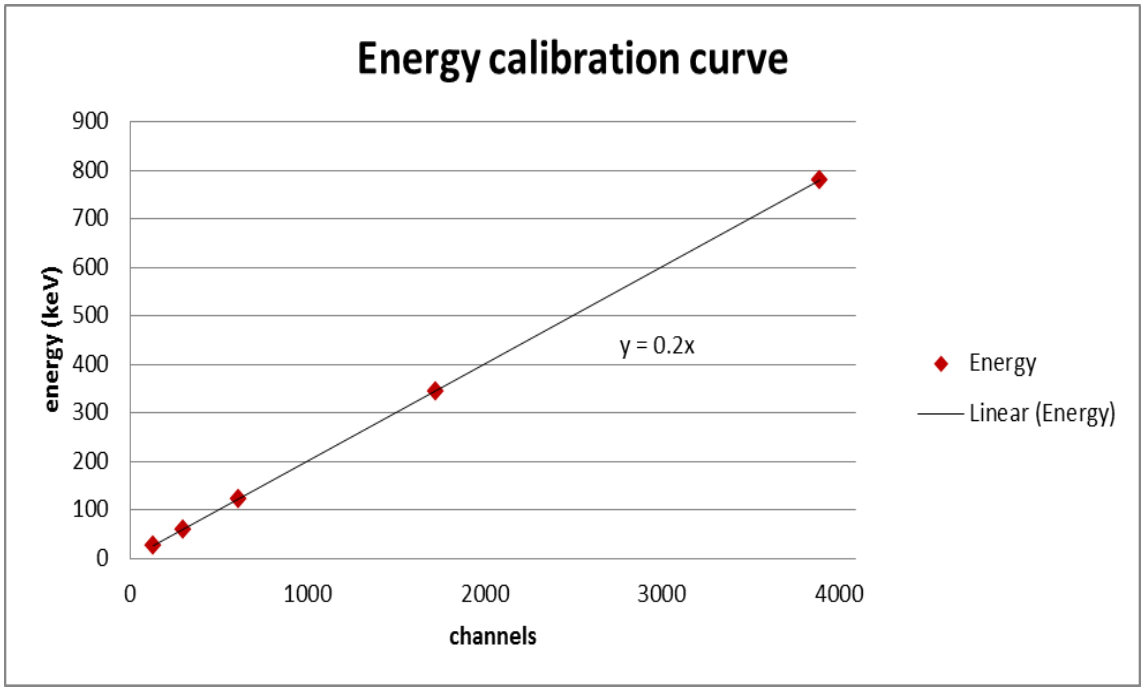

Figure 4.7: red detector energy calibration curve (4k setup)

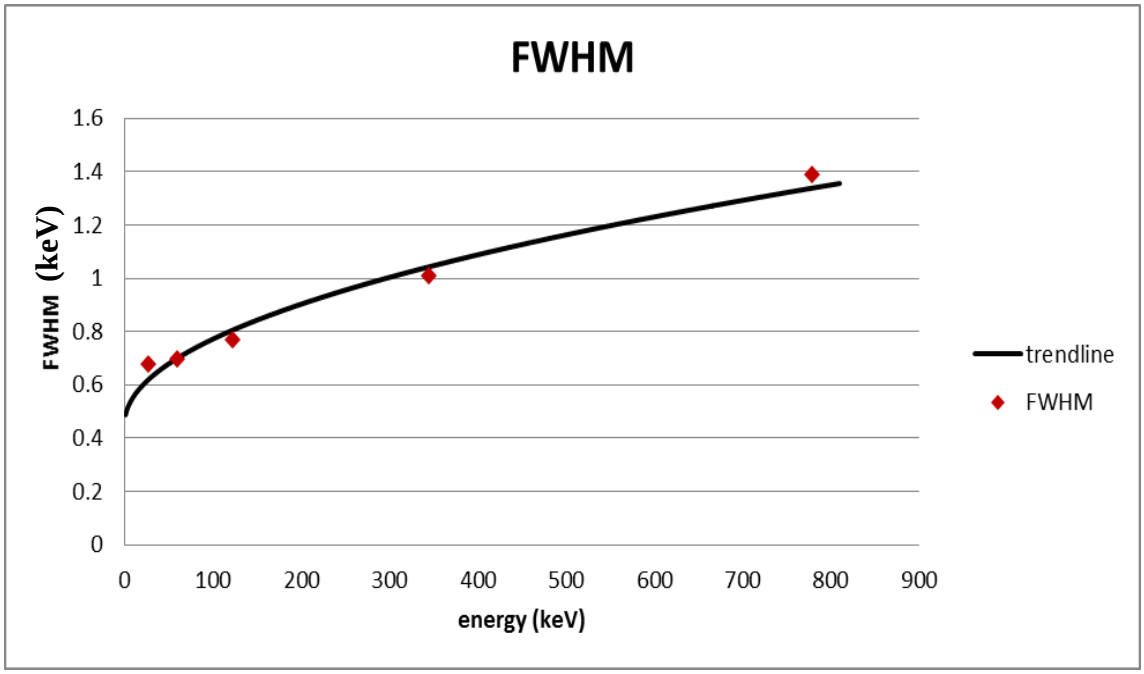

Figure 4.8: red detector resolution curve (4k setup)

4.3.3 Results for 8k channels

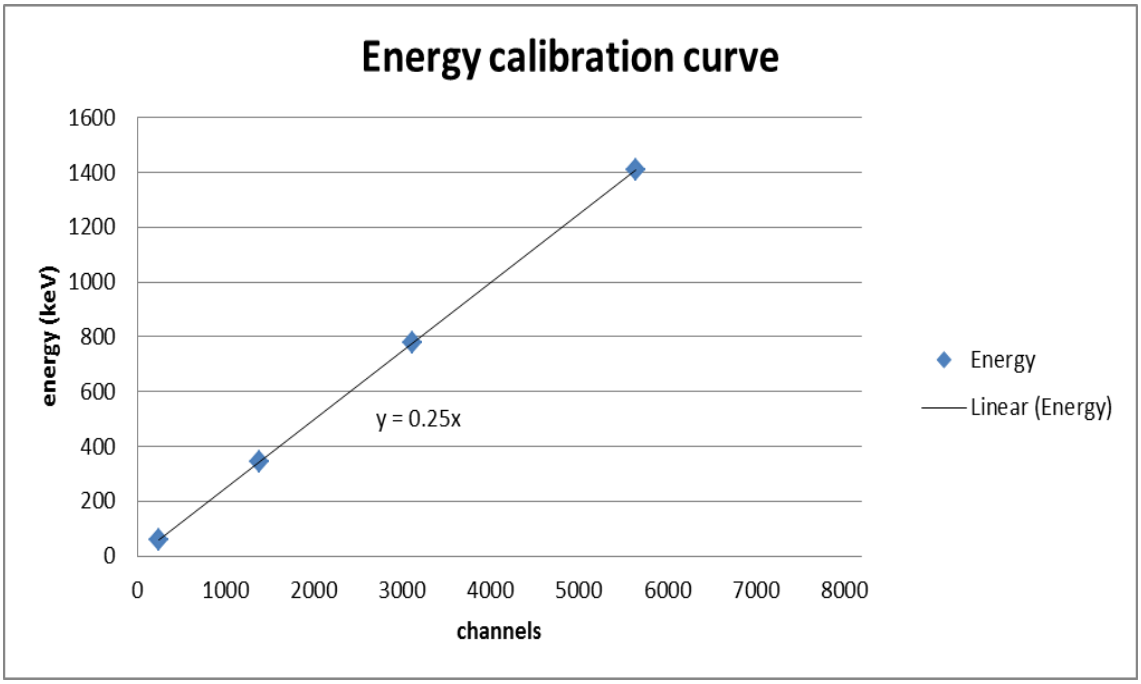

Figure 4.9: blue detector energy calibration curve (8k setup)

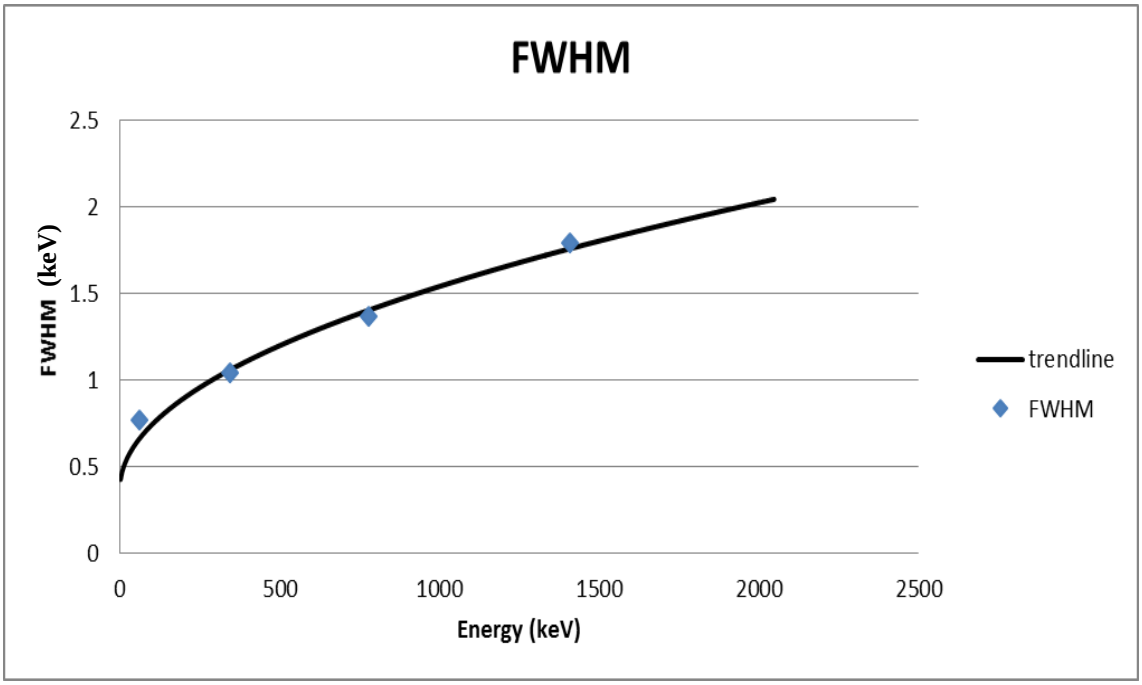

Figure 4.10: blue detector FWHM curve (8k setup)

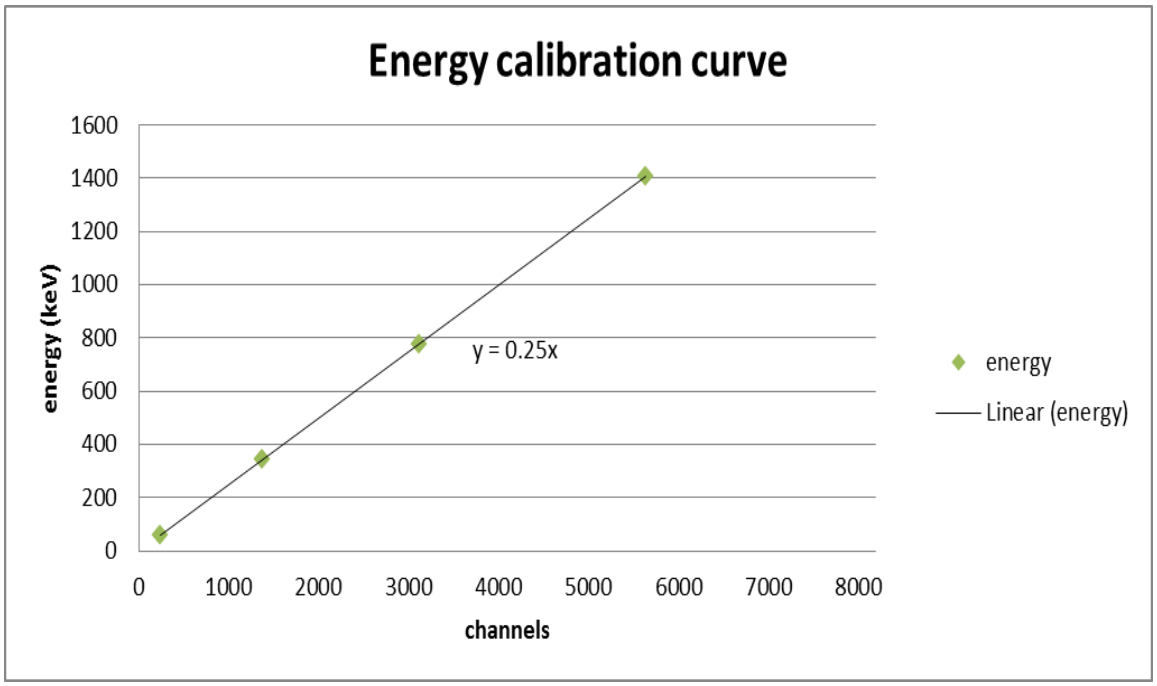

Figure 4.11: green detector energy calibration curve (8k setup)

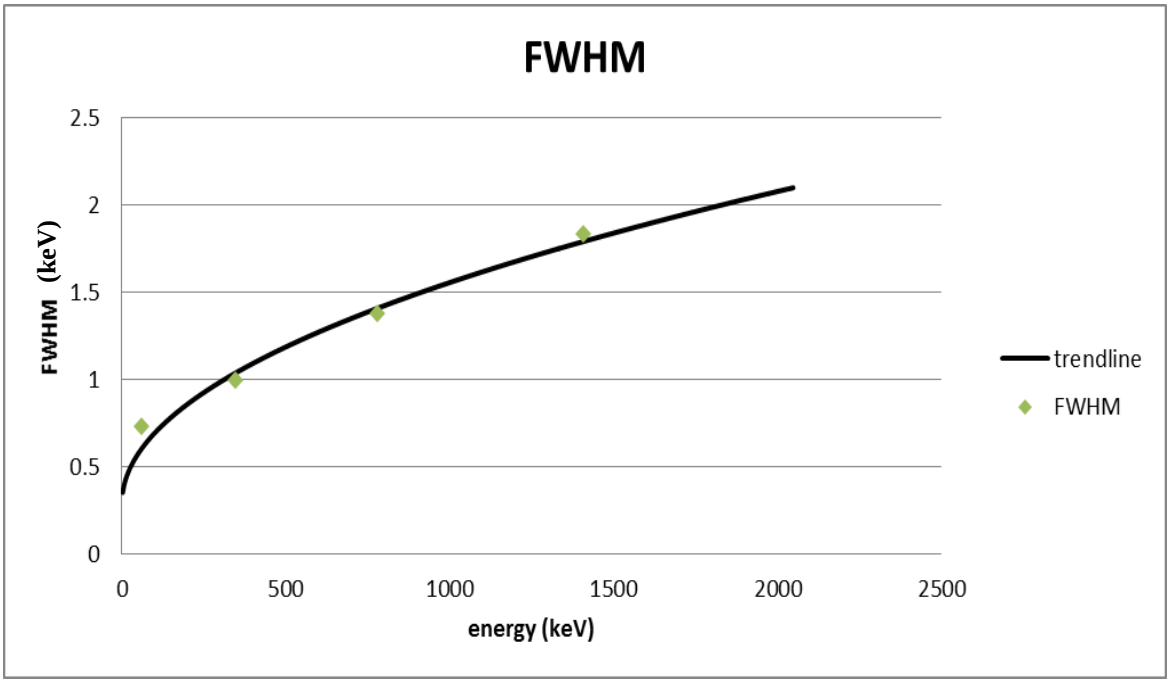

Figure 4.12: green detector FWHM curve (8k setup)

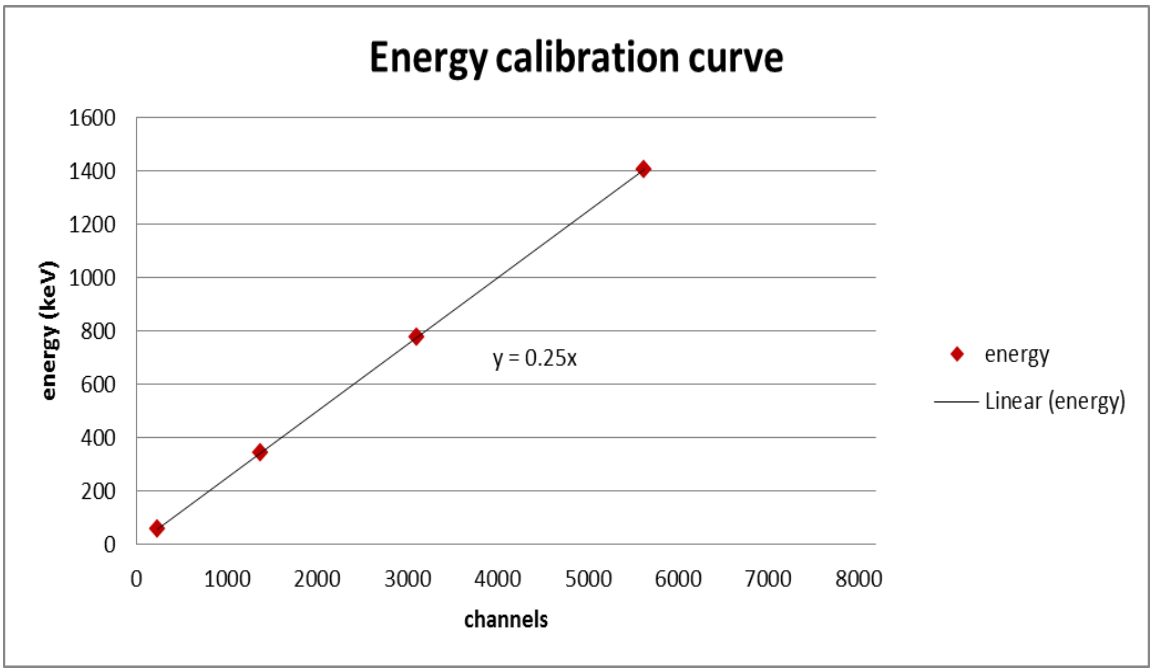

Figure 4.13: red detector energy calibration curve (8 setup)

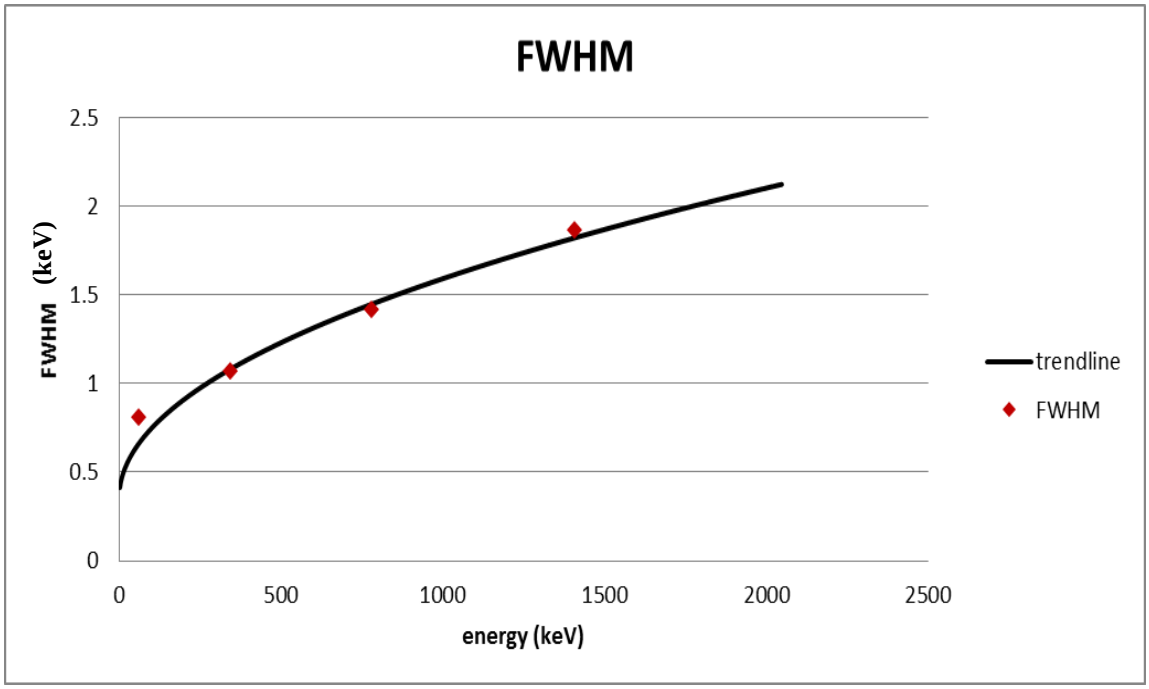

Figure 4.14: red detector FWHM curve (8k setup)

4.4 Quality Assurance measurements

4.4.1 Radioactive sources

For the Quality Assurance (QA), ^{152}Eu and ^{241}Am sources were used. These measurements are important to see if the detectors are stable during the time.
The europium source was the same as was used for the energy calibration and is the one with lower activity (30.1±0.4 kBq).
The americium source, instead, was different from the one for the energy calibration. Its activity at the reference date on 2003-03-11 is 87±8 kBq (Figure 4.15).

Figure 4.15: sources of ^{241}Am and ^{152}Eu used for QA

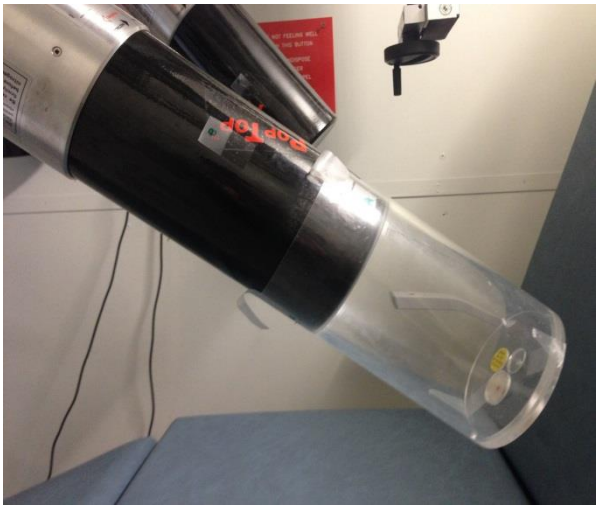

Figure 4.16: holder used for QA sources

4.4.2 Protocol for QA measurements

The sources were placed in a plastic tube at 25 cm of distance from the detectors (Figure 4.16) for 300 s for each detector. This was done because the conditions have to be always the same; in this way, it was possible to see if the detectors are stable or not.
The parameters to follow up were three:

- Peak Centroid: this is most useful for the operators, because they can see if there is a shift in the spectrum. So they can change the amplifier gain to restart the previous conditions;

- FWHM: this is important for the resolution of the detectors during the time; on the other hand, an increase in FWHM is often the first indication of a vacuum seal problem;
- Decay Corrected Area: this is the net area of the peak of interest that take into account also the decay of the radionuclide: $N_{dc,i} = \frac{N_i}{e^{-\lambda t}}$; this parameter is an indication of the detector efficiency stability with time.

At the beginning, the measurements (N=number of measurements) were done twice a day to reach a sufficiently large set of data to calculate the standard deviation:

$$\sigma_{FWHM} = \left[\frac{1}{N-1}\sum_{i=1}^{N}(FWHM_i - \overline{FWHM})^2\right]^{1/2} \quad \text{(Eq. 8)}$$

$$\sigma_{dc} = \left[\frac{1}{N-1}\sum_{i=1}^{N}\left(N_{dc,i} - \overline{N_{dc}}\right)^2\right]^{1/2} \quad \text{(Eq. 9)}$$

With this results it is possible to calculate the lower and the upper warning levels (±2σ), that correspond to a 95.4% confidence interval, and lower and upper action levels (±3σ), that correspond to a 99.7% confidence level. The data from the detectors should not exceed two consecutive warning levels or an action level (yellow and red lines in Figure 4.17 and 4.18).

The peaks taken into account for both setups (4k and 8k) are showed in Table 5 [11]

Table 5: Energy peaks used for QA check

4k setup		**8k setup**	
Energy (keV)	**Intensity (%)**	**Energy (keV)**	**Intensity (%)**
16.96	18.58	59.54	35.92
26.34	2.31	344.28	26.59
59.54	35.92	778.90	12.97
121.78	28.41	1408.01	20.85
344.28	26.59		
778.90	12.97		

4.4.3 Results

These are the results for the red detector at 59 keV peak. As it is possible to see in the figure 4.17 the resolution was decreasing (a bad resolution corresponds to an increase of FWHM) with the time. For this reason, a warm up of the detectors was performed (red vertical line) and after that, the resolution seemed to stabilize again. With the warm up

the detector's cooling was stopped and it was necessary to wait until the detectors reach again the environment temperature. Once that they are at this temperature, it was possible to recool them again up to the desired temperature. Same thing for the blue detector, even if its resolution was not decreasing as much as the red one. The green detector, instead, after the warm up, had a leakage current too high, maybe from a vacuum lost, so it was not possible to restart it again. The decay corrected area, instead, was almost stable for all the detectors during the time.

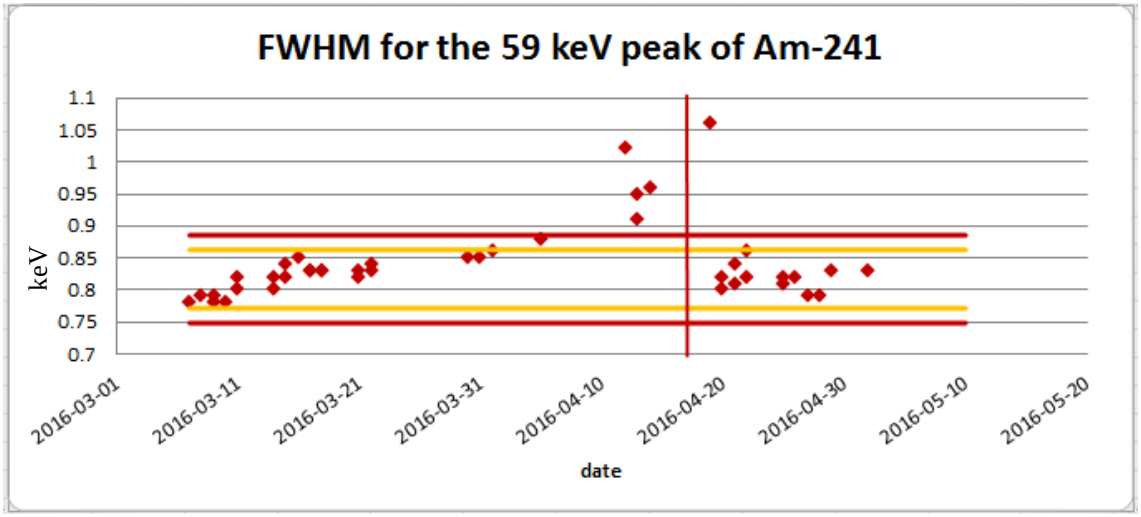

Figure 4.17: red detector FWHM in QA check

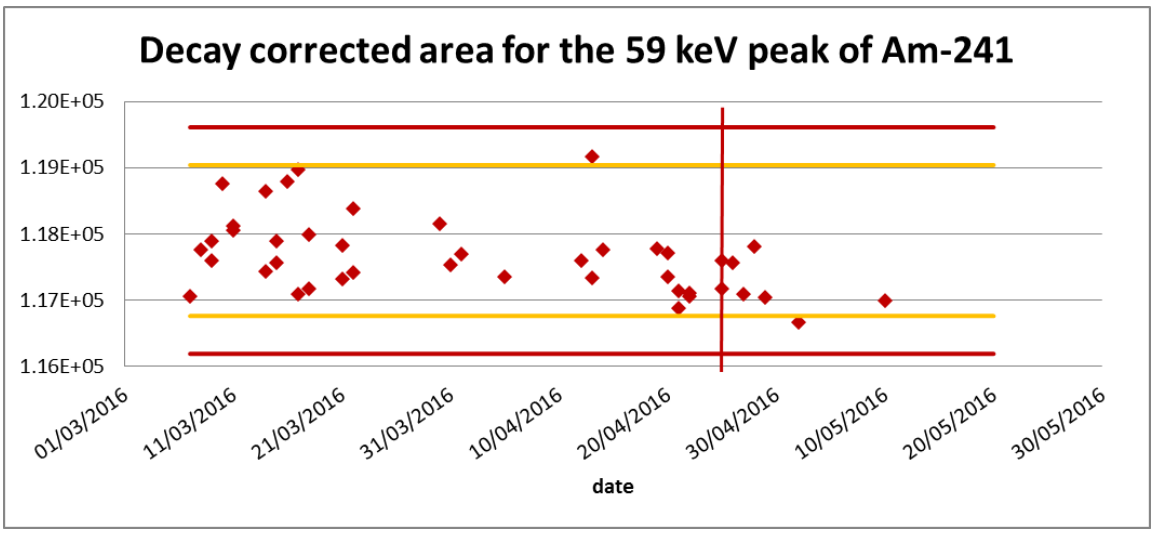

Figure 4.18: red detector decay corrected area check for QA

4.5 Efficiency calibration

4.5.1 Lawrence Livermore National Laboratory (LLNL) phantom

The LLNL phantom was used [12, 13] (Figure 4.19) for lung counting calibration. This phantom reproduces the tissues and organ placement of a human torso to simulate the interaction of low energy photons with bones, cartilage, and adipose and muscle tissues. It is made of muscle equivalent material and has synthetic cartilage and bone. Four different overlay plates are supplied with the torso. They are made of different adipose-muscle equivalent mixtures and they are needed to simulate a range of Chest Wall Thicknesses (CWTs). In the torso cavity, there are removable lungs, heart, liver, lymph node and two kidneys. All internal organs, except the lungs, are made of muscle equivalent material, while the lungs are constructed of lung equivalent material. In the phantom, there is also a rib cage, a spinal tissue block substituted for the spine [14], but the scapula is not present. The thickness varies from 16.1 mm (no overlay) to 40.5 mm (with the thickest overlay added) (Figure 4.20).

Each series of overlay plates simulates different adipose-muscle composition:

Figure 4.19: LLNL phantom overview

Figure 4.20: overlays of LLNL phantom with different chest wall thicknesses

- Series A: 87% adipose and 13% muscle;
- Series B: 50% adipose and 50% muscle;
- Series C: 0% adipose and 100% muscle.

The proportions of these overlays have to be combined with the composition of the torso (100% muscle) and then the final combined compositions are:

- 15% adipose and 85 % muscle for series A;
- 48% adipose and 52% muscle for series B;
- 100% for the series C.

For this efficiency calibration, Series B overlay plates have been used.
Features of the torso and of the overlays used are explained in the Table 6.

Table 6: LLNL phantom data

Phantom		**Thickness (mm)**			
Part	**Number**	**Left chest (mm)**	**Right chest (mm)**	**Left + Right chest (mm)**	**Liver (mm)**
Torso	C-133	15.4	17.0	16.1	14.8
Overlay	B-139-1	7.0	7.2	7.1	7.2
Overlay	B-139-2	12.0	12.2	12.1	12.1
Overlay	B-139-3	17.4	17.5	17.4	18.1
Overlay	B-139-4	24.3	24.5	24.4	23.5

A pair of non-radioactive lungs was provided with the phantom, together with three additional pairs of lungs contaminated lungs by ^{241}Am, ^{239}Pu and ^{152}Eu for the calibration. The total reference activity of the lungs was 22.57 kBq on 1985-01-07 for americium, 181.3 kBq on 1983-10-01 for plutonium and 42.58 kBq on 2014-07-30 for europium.

4.5.2 Counting protocol

The LLNL phantom was counted with and without the B-series overlays plates. The detectors were positioned in front of the phantom (Figure 4.21). The smallest distance between the detectors and the torso is about 1 cm. All counting times were sufficiently long to obtain low uncertainty counting statistics at the energies of interest. Data were

collected for individual detectors and then summed. All the results are presented for a two-detectors array. In Table 7 it is possible to see the energy peaks used to obtain the efficiency curve, with their respective intensities.

Figure 4.21: position with 2 detectors

Table 7: Peaks used for efficiency calibration

Radioisotope	Energy (keV)	Intensitiy (%)
^{241}Am	16.95	18.58
^{241}Am	26.345	2.31
^{239}Pu	38.661	0.01
^{239}Pu	51.624	0.03
^{241}Am	59.541	35.92
^{152}Eu	121.78	28.41
^{152}Eu	244.7	7.55
^{152}Eu	344.28	26.59
^{152}Eu	778.9	12.97

Background measurement was done with the phantom on the chair, with not radioactive lungs inside, for a time of 60000 seconds. The detectors were placed in front of the phantom.

5 MCNP SIMULATIONS FOR EFFICIENCY

5.1 Introduction

MCNP simulations were used basically to find the best position for the detectors, since we wanted to have the highest efficiency achievable. Detectors and phantom were simulated in different positions and the counting of the photons reaching the detectors was found. Two best positions were established, one with all the three detectors and the other with only 2 detectors (because one was broken). MCNP was used also to see the efficiency uncertainties coming from changing the distance between the detectors and the chest and changing the size of the lungs. In these last simulations, a new phantom model, more similar to a person, was used.

The Monte Carlo code used in this work is MCNPX^{TM} version 2.7.0. It is a general purpose radiation transport code designed to track many particle types over broad ranges and energies [15]. This code can be used for many applications, like radiation shielding, personnel dosimetry, reactor design and detector design and analysis. MCNP gives the normalized number of particles interacting with a detector. This normalized tally is the counting efficiency of the detector measured in units of counts-per-second per photon-per-seconds, or directly counts per photon. The relative error is given with the tally and it is equivalent to the inverse square root of the number of the histories contributing to the tally. Relative errors of 0.1-0.2 suggest that the tally result is questionable [16]. Tally results above 0.2 are not meaningful but are generally reliable for a relative error less than 0.1 [17].

5.2 LLNL Phantom and HPGe detectors

5.2.1 Models

The virtual torso was based on a torso section of the IAEA Phantom- LLNL phantom (Figure 5.1, views performed with a visualisation program-*Moritz* [18]). The view of the phantom was mirrored with the respect of the reality; so the right lung was on the left (green one in the figure) and the left one was on the right (blue one in the figure). Lungs were filled with lung tissue, ribs with skeletal bone and the other parts with soft tissue, with composition of 83% muscle and 17% adipose tissue (Table 8). This was done because the thickness of the chest wall in the input file was equivalent to the one of the torso plus the first overlay of 0.7 cm.

Table 8: Phantom composition

Soft Tissue	**Value**
Density	1.062 g/cm^3
Composition	**Mass Fraction**
H	0.095
C	0.599
N	0.029
O	0.260
Ca	0.014

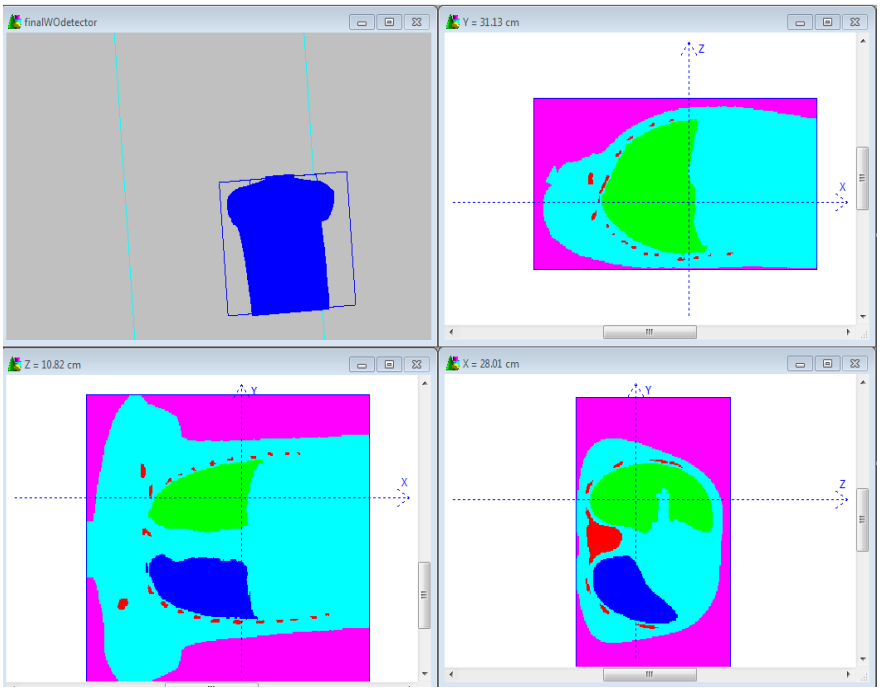

Figure 5.1: wiew of LLNL phantom from *Moritz*

The Ortec Detectors models were available and they were modelled based on specifications supplied by EG&EG Ortec and through some radiographies and several analysis (Figure 5.2). The detectors were simulated in faithful way with all their parts, including the dead layer.

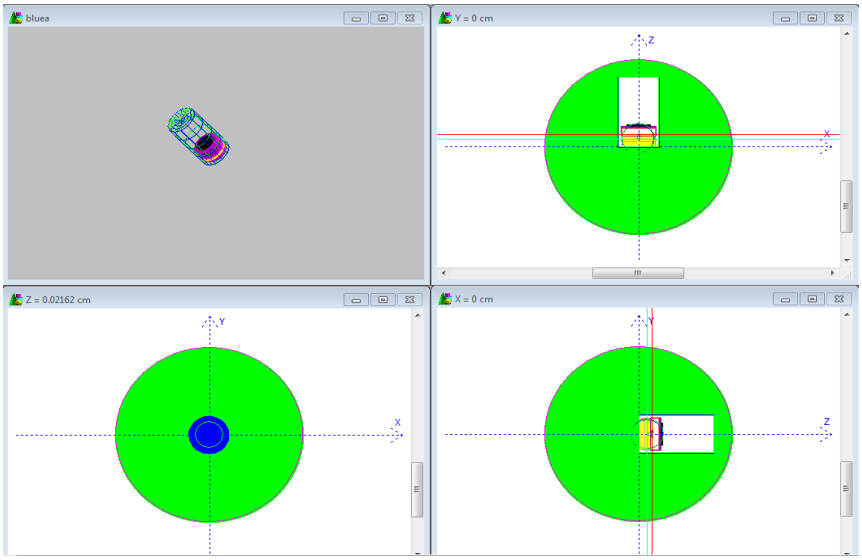

Figure 5.2: view of detector from *Moritz*

5.2.2 Validation of the model

To validate the model, the detectors were put in a position easy to reproduce in the reality (Figure 5.3). With two measurements, one with two detectors and one with the other, it is

Figure 5.3: validation of the model

possible to see that the model (of detector and phantom) simulated with MCNP and the reality is quite similar (Table 9). The obtained results justify the validation, then.

Table 9: Validation data

Detectors	Measurements		Simulation	Difference between measurements and simulations
	Net Peak Area	Efficiency (59 keV)	Efficiency (59 keV)	
Red	9158	3.96E-03	3.97E-03	0.25%
Blue	7320	3.13E-03	3.14E-03	0.44%
Green	7983	3.45E-03	3.46E-03	0.32%

5.2.3 Best position

Several positions were simulated to find the best position for the efficiency of the detectors. Particularly, 14 positions for the entire setup were simulated.

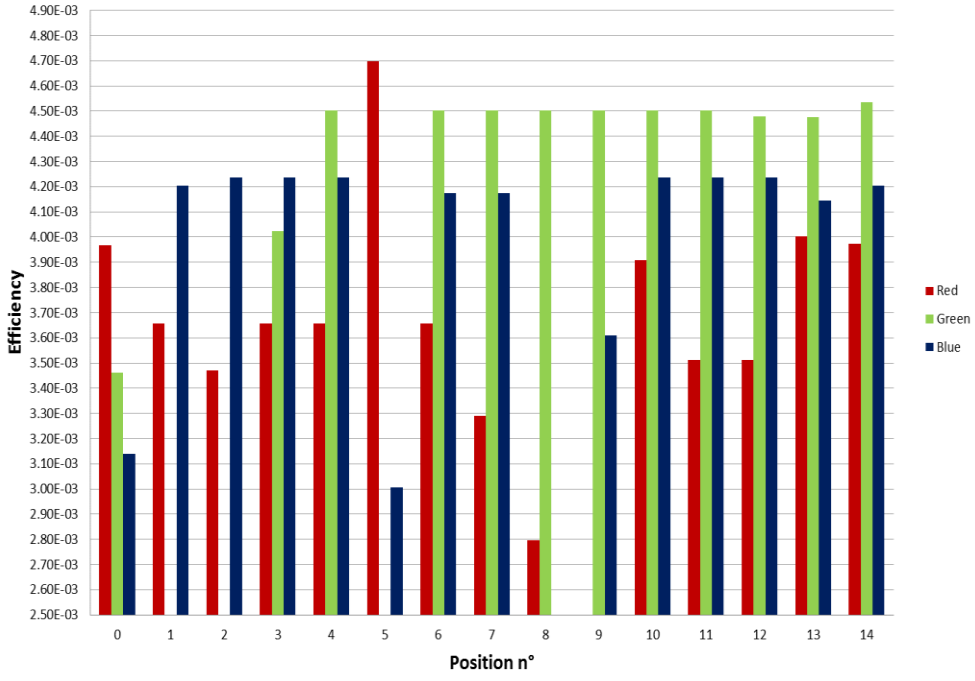

Figure 5.4: graph of the efficiency depending on the position

Starting from an input file with the three detectors located in the origin of the axis, each time the positions of them have been changed, through translations and rotations around the axis. As we can see in the figure 5.4 the best position for the red detector should be the number 5, but it is possible to use this position, only if there was only one detector in front of the right lung. Since we have two detectors on the right lung, the best position for the red one is position number 13. The blue and the green detectors have very similar efficiencies in different positions. It is possible to choose between many options, then.
Two setups, with the highest efficiency and also easier to reproduce in reality have been chosen, one with only two detectors and the other with all the three ones. In the first case, the positions are the number 5 for the red detector and the number 4 for the blue one. With the three detectors, the positions chosen are the numbers 13, 4, 14 respectively for the red, blue and green detector.
In the figures below (Figure 5.5 and 5.6), it is possible to see the positions found with the simulations and the real positioning in the bunker.

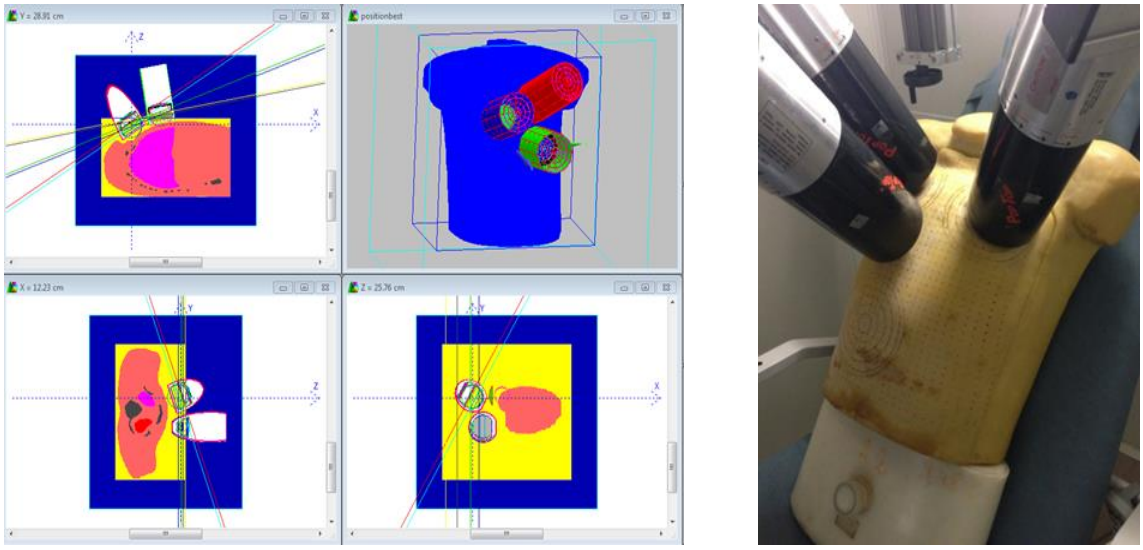

Figure 5.5: best position for three detectors

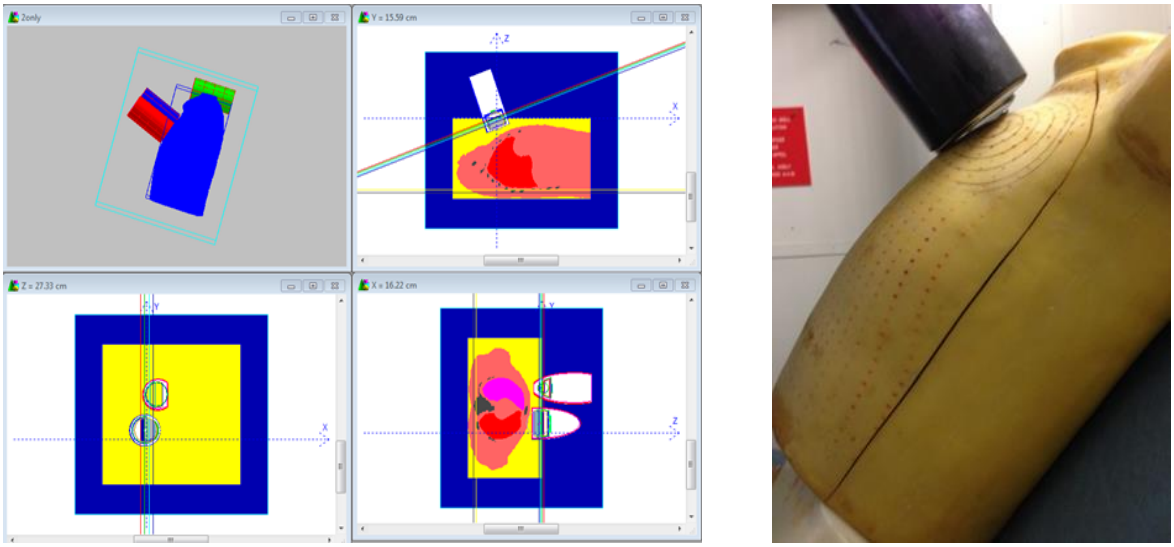

Figure 5.6: best position for two detectors

5.2.2 Comparison with measurements

By comparing the measurement results obtained with the LLNL phantom and the simulation of the same setup, it is possible to see a difference of 0.77% at energy of 59 keV (Figure 5.7) and about the same percent value at 26 keV, but for the other energies, the differences are higher. This discrepancy can come from a difference in position between the measurement and the simulation, maybe the position was not exactly the same of the simulation. The right explanation is a not perfect position of the detector during the measurement, also because, to change the radionuclide, the phantom had to be repositioned every time. Anyway, the simulations were important to see the trend and behaviour of the detector efficiency, and for the energy of interest (59 keV) it works well. In this way the curve seems optimized for the low energies, actually the energies of our interest.

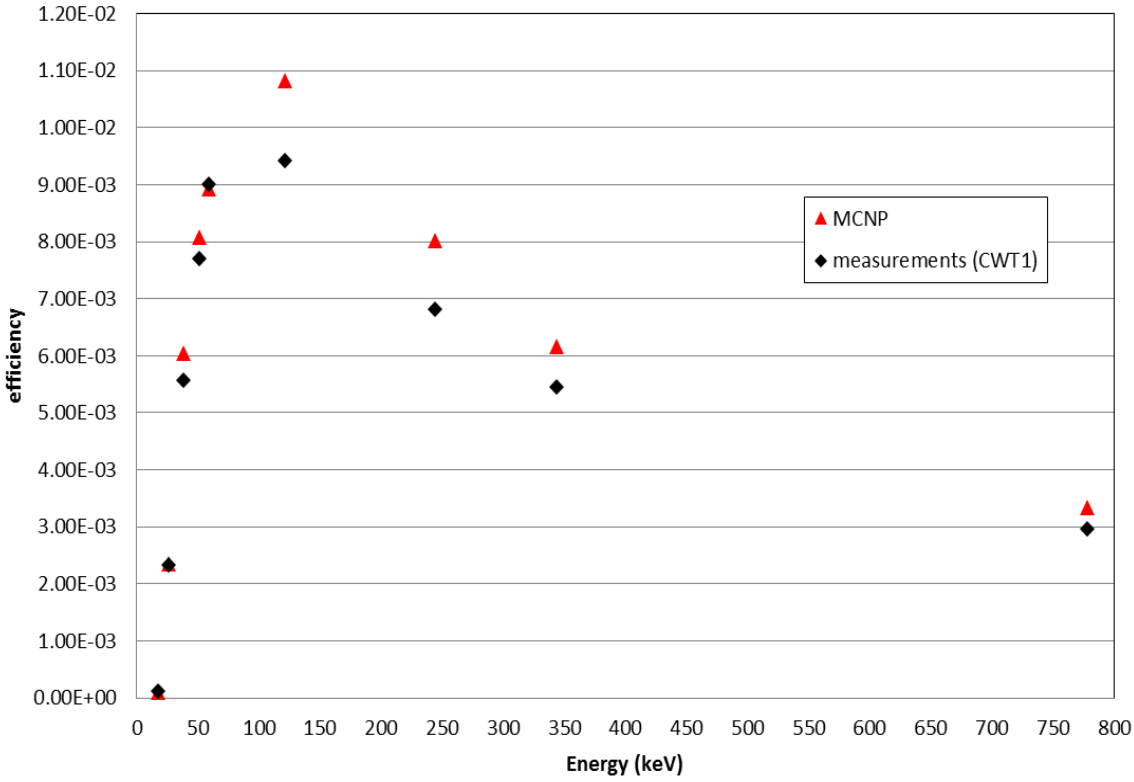

Figure 5.7: difference between MCNP simulations and measurements

6 MEASUREMENTS RESULTS: EFFICIENCY CURVES

The graph in Figure 6.1 and 6.2 shows the efficiency curves found in all the measurements done with the LLNL phantom. These curves are the sum of the spectra of the two detectors, named Blue and Red. Since there were not peaks in the energy range between 60 and 120 keV, we can expect that the efficiency curve raises until 121 keV (^{152}Eu) and then starts to decrease or it raises until about 100 keV and then starts to decrease. All the five curves, depending from the thickness of the overlay used, have the same trend.
The curves used to fit the data have the trend

$$\ln(\varepsilon) = c_1 + c_2 \ln(E) + c_3 (\ln(E))^2 + c_4 (\ln(E))^3 + c_5 \ln((E))^4 + c_6 \ln((E))^5 \quad \text{(Eq. 10)}$$

Where the c_1, c_2, c_3, c_4, c_5, c_6 are coefficients calculated from the Genie software and E is the energy in keV.

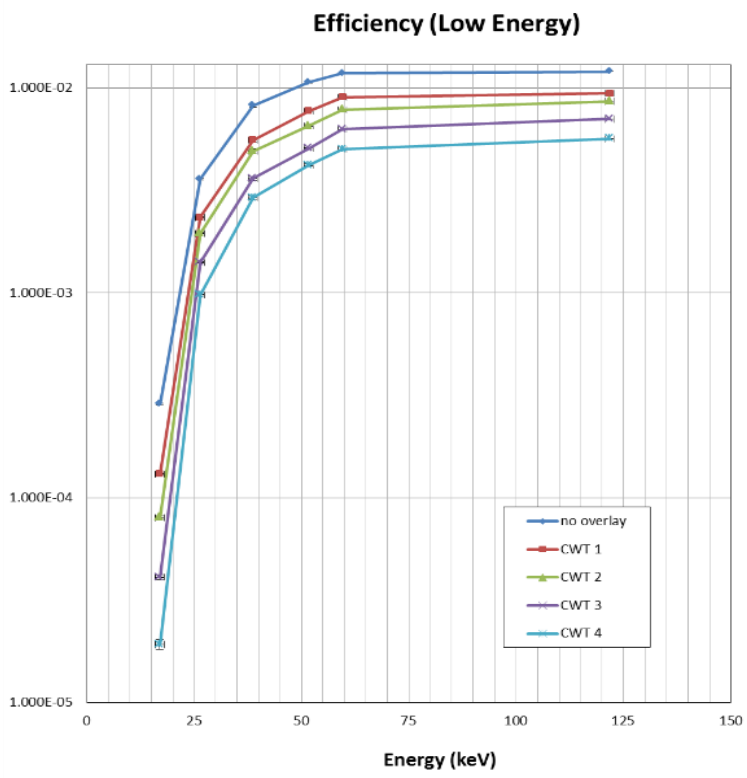

Figure 6.1: efficiency at low energy (up 121 keV)

These curves have been saved in different calibration files and, when the measurement is done, one of this file, depending from the chest wall thickness of the person, is loaded. Figure 6.5 gives only the fitted curves, as they will be used. In the figure 6.3, I put also the uncertainty bars, but they are hided by the scale of the graph. They represents just the uncertainty of the peak area, values calculated by the software Genie. The uncertainties values are about 0.1-0.5 %, with some exceptions, as 5% at 17 keV for the thickest CWT. The curves seem to increase for energy greater of 779 keV, but this is no issue for our purpose, because we are interested in the low energy range, especially 59 keV of ^{241}Am.

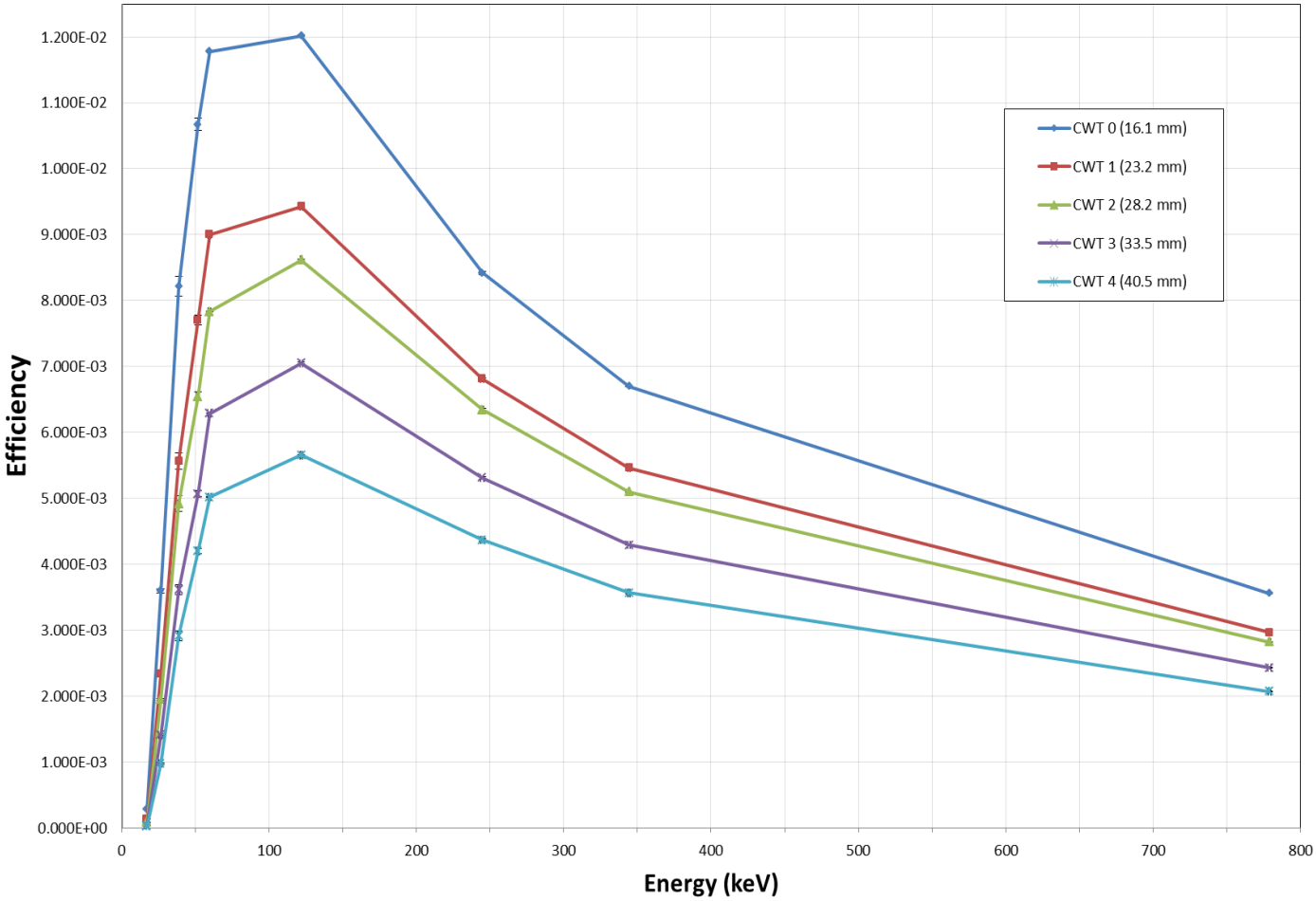

Figure 6.2: efficiency curves for different CWT.

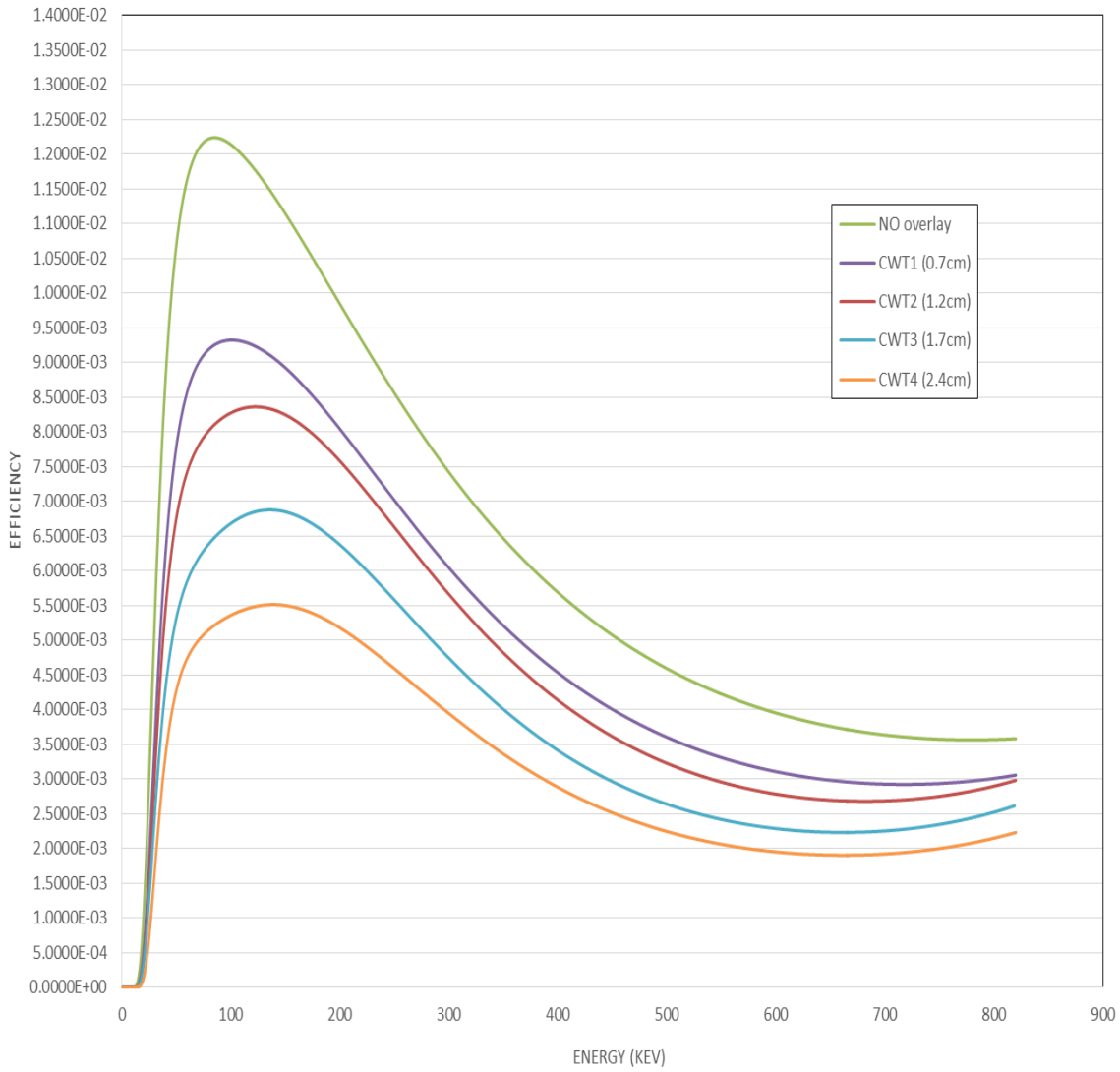

Figure 6.3: efficiency curves trend in *Genie2000*

6.1.1 Comparison with actual setup

In the graph below (Figure 6.4) it is possible to see the differences between the actual setup, with the two LEGe detectors on the right lung, and the new setup, with the two HPGe detectors, one above each lung. The difference between the two setups, considering the measurement with the LLNL phantom without overlay, is clear and the efficiency is clearly improved with the new setup, as it was expected. Considering the 59 keV peak of americium and the 121 keV peak of europium, we have an efficiency increase of respectively 115 % and 74%.

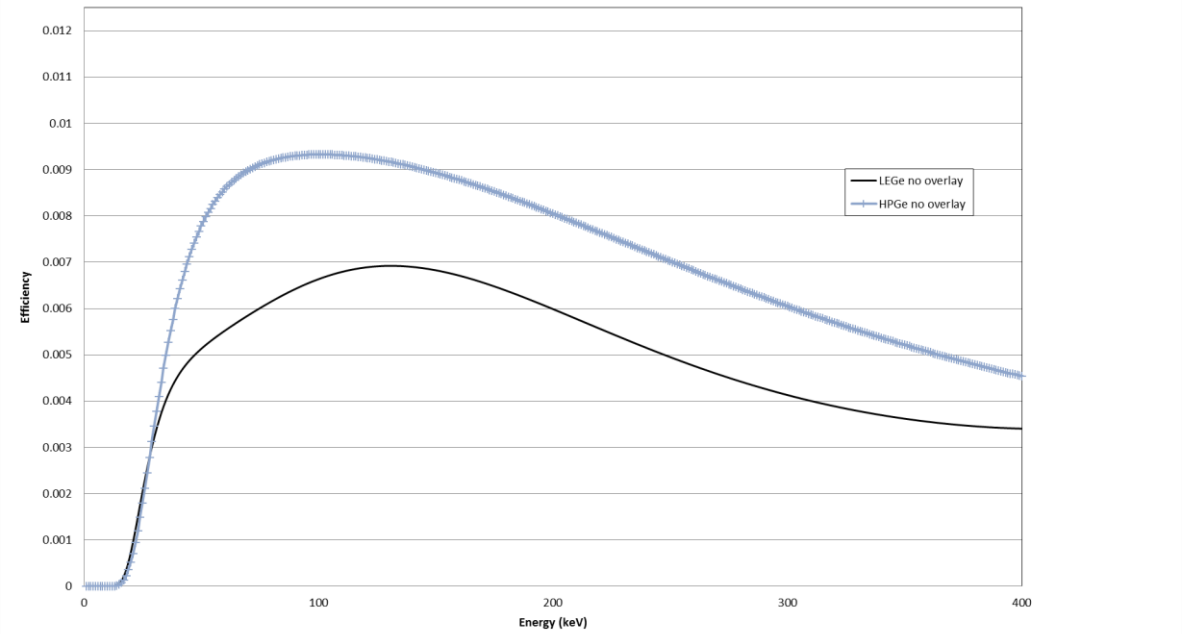

Figure 6.4: comparison between HPGe and LEGe efficiency curves

7 UNCERTAINTIES ANALYSIS AND DETECTION LIMITS

7.1 Introduction

Uncertainties have to be taken into account, especially counting uncertainties, about the peak area, and efficiency uncertainties. Once the efficiencies curves are found, it is needed to take into account that a person will measured, not a phantom. Then many uncertainties on the measurements have to be considered, for example, the person can move a little bit, since the measurement takes 50 minutes. In addition, one has to consider that the formula to evaluate the CWTs is not perfect; then uncertainty should be taken into account for this value. Moreover, there could be little differences if the operator does not put the detector in the right position, so the distance between the chest of the person and the detectors will not be the same as during the calibration. For this reasons, additional measurements were done to evaluate of the related uncertainties. In these measurements the phantom without overlay (CWT 0) and the phantom covered with the thickest one layer (CWT 4) were used.

The uncertainty of the source intensity values and the uncertainty on the measurement time were considered negligible. It was possible to do that because the peaks of interest were very intense so their intensities have an uncertainty less than 0.5% [11].

The phantom that was used for the calibration was composed of a hull and a plurality of plates. Although the lungs of different people vary in volume, geometry and position of the hull of this phantom is considered representative for the persons who are undergoing a lung measurement. The deviation in efficiency that may result from the use of this phantom, especially for people who are very different from this standard trunk, were not considered in this study.

7.2 Counting uncertainties

The uncertainty on the peak area, calculated directly from the peak analysis on Genie2000, is considered < 1%. Anyway the software will evaluate the counting statistics for each measurement (and each peak) independently and they will be taken into account together with the uncertainty on the efficiency curves.

For routine lung measurements to determine ^{241}Am, a sequence analysis was prepared in Genie. In this way, the operator's influence in the analysis can be considered negligible.

Repetition measurements were carried out: the same operator (Figure 7.1 and 7.2) has repositioned the phantom (CWT0 and CWT4) two times. The standard deviation of these measurements (peak area) divided by the average value indicates the repeatability (Table 10). The maxima values found are 2% for the CWT0 and 3% for the CWT4.

Table 10: Repetition uncertainties

E(keV)	Uncert. CWT0	Uncert.CWT4
26	3.80%	2.18%
59	1.91%	3.19%
121	1.03%	2.15%
244	1.30%	2.08%
344	1.48%	2.10%
779	0.88%	1.98%

If nuclides which have peaks close to background peaks are present in the body, then they can cause problems for the correct determination of the peak area of the considered radionuclide. Depending on the resolution at the considered energy, the peaks will overlap partially or almost completely so it will be difficult to see that these are two peaks. In addition, the Compton contribution of a background line may interfere in the determination of the peak area of another peak located at a lower energy.

The software Genie will correct the peak area for occurring interferences. The greater the activity in the body, the more accurate it will approach the actual peak area of the searched nuclide. When two peaks in the spectrum are indistinguishable because of an interference, they are not used for the calculation of activities in the body. Genie takes this also into account in determining the uncertainty.

The activities to be put into phantom for preparing the calibrations were relatively high compared to the activity measured positive in people. The dead time for the calibration measurements was never greater than 1%. For routine measurements in which no lung radionuclides to be detected, the dead time is less than 0.1%. The required measuring time is entered in Genie as "live time". This takes into account the dead time, which is

compensated. The live time was therefore equal to the real time plus the time when no pulses could be registered.

7.3 Efficiency uncertainties

In the formula used for efficiency calculation the quantities *A* and *N* relate to the calibration measurements, not on the measurement of a person. Therefore, many uncertainties had to be considered.

The uncertainty on the number of counts was affected by the counting statistics. The greater the peak area, the smaller is the uncertainty. On the other hand, there are also other parameters such as the motion of the person during the measurement, the influence of the positioning of the person relative to the detectors by the operator (mainly the distance between the thorax and the detectors).

The duration of the acquisition for calibration measurements is, in principle, selected so that the considered peaks having a peak area of 10 000 counts. The statistical uncertainty (Poisson counting statistics) of the peak area wass then equal to 1%. In practice, it was ensured that the most significant peaks of ^{241}Am (59.5 keV) and ^{152}Eu (121.8, 244.7 and 344.3 keV) have a peak area of more than 10 000 counts. This uncertainty was considered 1% in the total uncertainty with a Poisson distribution.

The distance between the chest and detectors was fixed at 1 cm for the calibration measurements. This means that this must be the shortest distance between the thorax and one of the two detectors. As it is possible to see from the pictures of the position in the previous chapters, it is clear that the distance between the thorax and detector is not constant over the considered thorax area. As it is difficult to set accurately the distance in an actual measurement and because the curvature of the body of each person is different, and certainly does not correspond exactly to the curvature of the used phantom, it is clear that the distance is an additional uncertainty contribution. In order to determine it, measurements were carried out with ^{241}Am and ^{152}Eu lungs. In order to see also the influence of the chest wall thickness, different chest plates, plate 0 and plate 4, were considered.

The variation of the efficiency with the distance between detector and chest is plotted in the graphs below. It is clear that, for all energies, the greater the distance is between the detector and the chest, the lower the efficiency is (Figure 7.1 and 7.2).

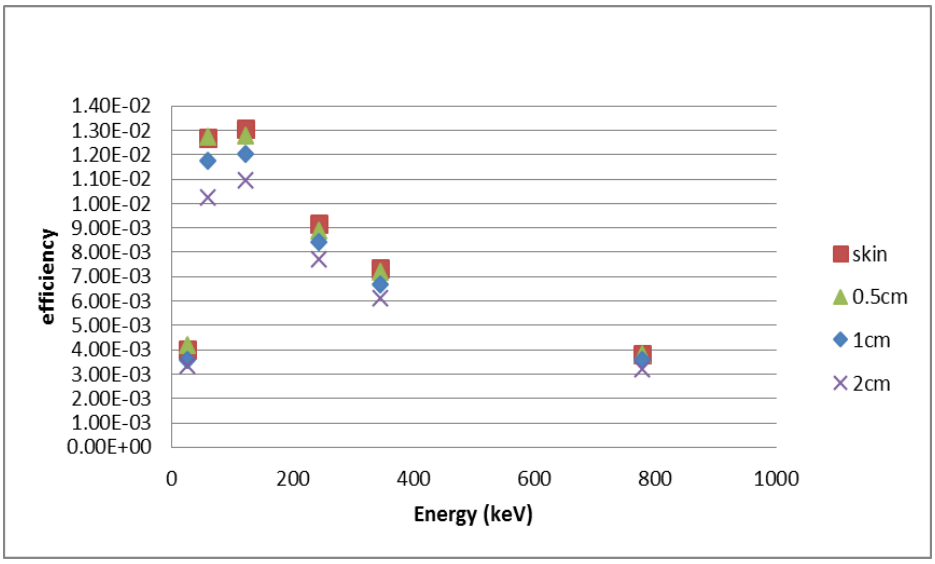

Figure 7.1: uncertainties changing the distance between detectors and chest for CWT0

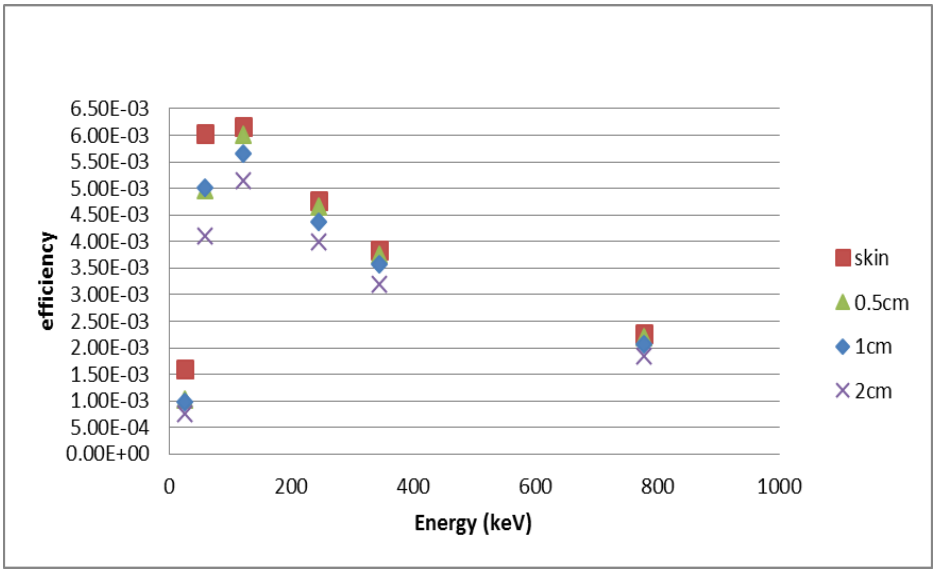

Figure 7.2: uncertainties changing the distance between detectors and chest for CWT4

A variation of the distance starting from the contact with the skin to 2 cm (distance between the chest and the detectors) was a realistic assumption, taking into account the different causes that may cause such a distance deviation. When all the points for the various chest plates are shown for this interval, may be seen that a deviation in efficiency of - 16% and +12% for the CWT0 and of -22% and +20% for the CWT4 are to be taken into account. This uncertainty was considered rectangular. When the distance between

the detector and the chest was 10 ±10 mm this entails an uncertainty on the efficiency of 14% ((16 + 12) / 2) for the CWT0 and 21% ((22+20)/2) for the CWT4. This gives a contribution to the overall uncertainty of 8.1% for the CWT0 and of 12.1% for CWT4.

Despite of the small freedom of movement of a person during a lung measurement, most people tend to sag in the chair and also to go to the right or to the left during the measurement in order to find more support on the armrests. The measurement position of the new setup, where the person is sitting in a tilted chair – almost lying- was chosen to minimize this movement. Nevertheless, in order to take into account the influence of this movement, it was simulated with the phantom.

A realistic estimate of the anomalies was a maximum displacement of ±1 cm in height and in moving to the right or left. The difference in height was simulated by changing the height of the detectors (Figure 7.3 and 7.4). The movement on the right or on the left was simulated by changing the position of the phantom in the two directions (Figure 7.5 and 7.6)

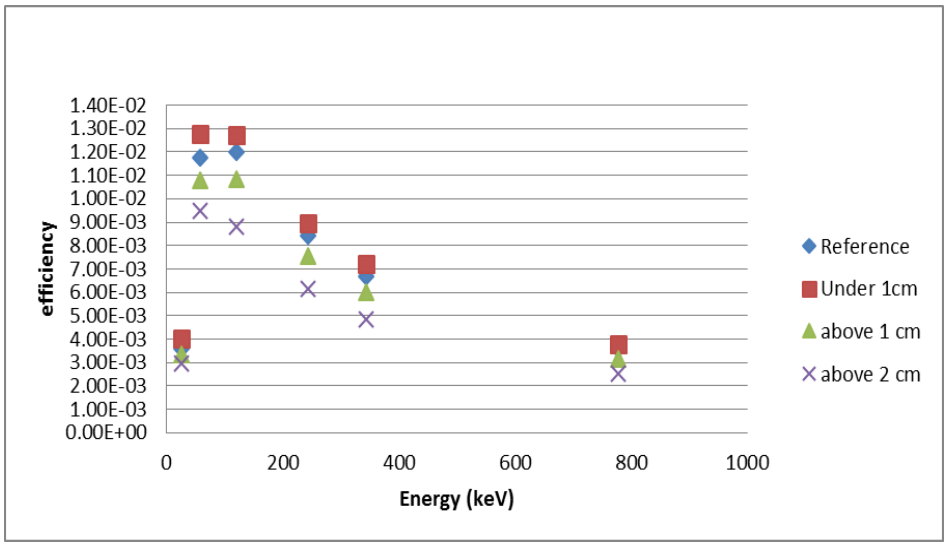

Figure 7.3: uncertainties changing the height of the detectors for CWT0

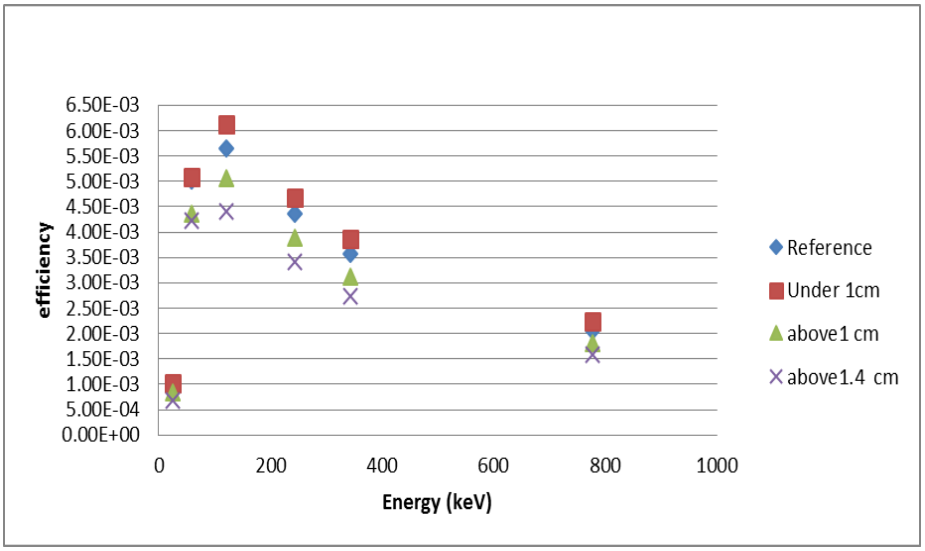

Figure 7.4: uncertainties changing the height of the detectors for CWT4

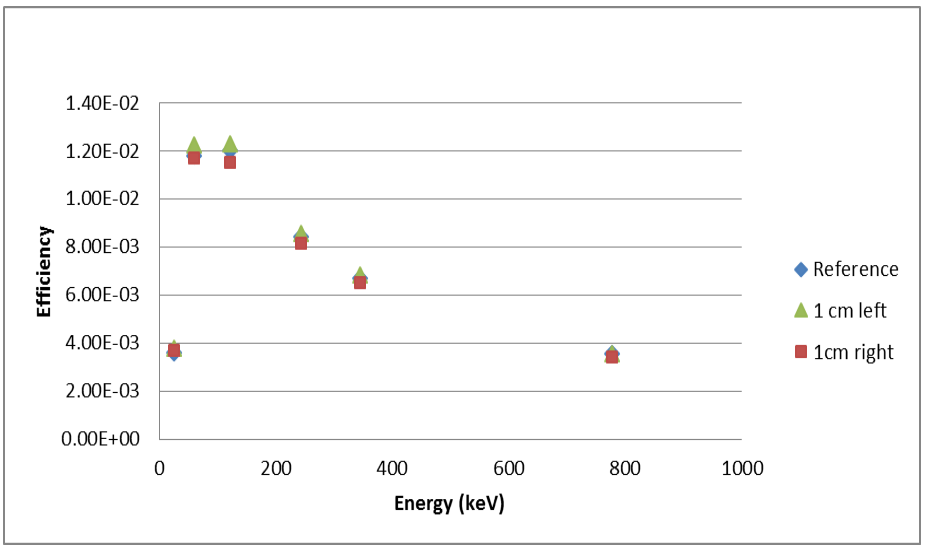

Figure 7.5: uncertainties changing the position of the phantom to the right and to the left for CWT0

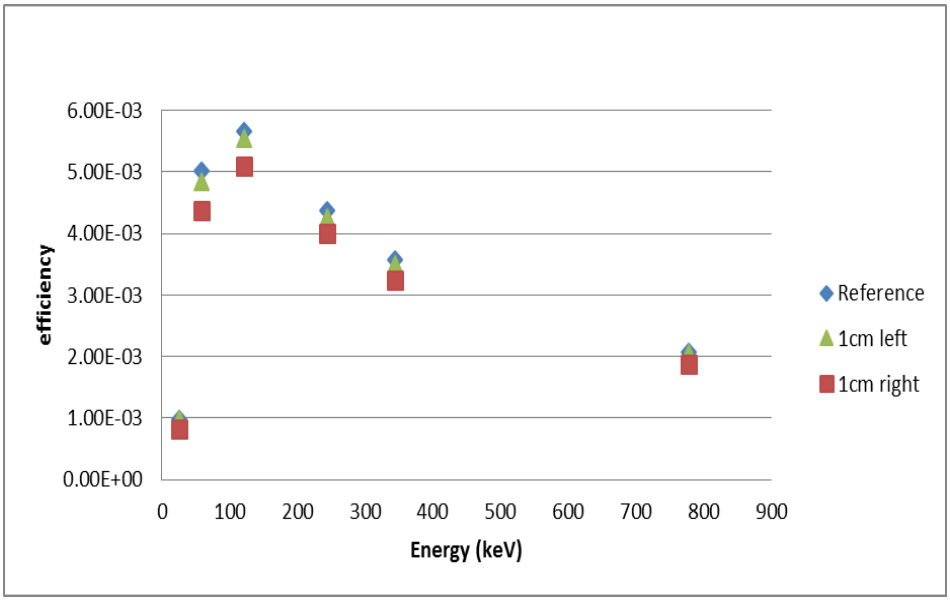

Figure 7.6: uncertainties changing the position of the phantom to the right and to the left for CWT4

^{241}Am peak at 59 keV gives a maximum deviation of -19.7% for 1 cm sag with CWT0 and -15.5% for 1.4 cm sag with CWT4,. while the ^{152}Eu peak at 122 keV shows a maximum deviation of -26% for 2 cm sag with CWT0 and -22% for 1.4 cm sag with CWT4. For the movement of ±1cm to the right or to the left the maximum deviation was 4.1% for the 59 keV peak and 4.3% for the 121 keV peak with the CWT0, while it was 12.9% for the 59 keV peak and 10 % for the 121 keV peak with the CWT4.

It was added an uncertainty of -26% for the CWT0 and of -15.7 % for CWT4 in the uncertainty budget. A triangular distribution was assumed. This gives a contribution to the overall uncertainty of 10.6% and 6.4 % respectively.

7.4 Source activity uncertainties

The phantoms and related sources used for this calibration were borrowed from the IAEA (two pairs of lungs contaminated with Am-241 and Pu-239) and from IRSN (a pair of lungs contaminated with Eu-152). The specifications of these lungs were reported in the paragraph 4.5.1.

The activities were added and corrected to the day of the measurement. The uncertainty on the source activity was given on the datasheet with a conservative value of 1%.

7.5 Uncertainty in the chest wall thickness

When a recorded lung gamma emission spectrum has to be analysed, a proper efficiency calibration has to be loaded first. This was obtained by an interpolation between two of the five reference efficiency calibration curves. This interpolation was done based on the chest wall thickness of the measured person, which is calculated using the formula Eq.7. In the efficiency calibration used, the uncertainty on the calculated CWT provides an additional uncertainty.

To evaluate the uncertainty on the efficiency, it was supposed a deviation of 3 mm in the CWT in which the effect is greatest. It makes sense that an error of 6 mm on a small CWT has greater impact than on a larger CWT. The top of the efficiency curve of 16.1 mm CWT has an efficiency of 0.0122. The efficiency for a cwt of 23.2 mm at the same energy is 0.0093. The difference between the two values is -24%, which was introduced in the total uncertainty.

This value is more than an overestimate of the actual uncertainty but the average deviation is difficult since it would have to be calculated for all energies and for each curve.

7.6 Uncertainty in efficiency curve fitting

When the efficiency calibration curve is calculated by Genie code, one obtains a fifth degree equation of the efficiency as a function of the energy. The average deviation of the points from the obtained curve was taken as the uncertainty on the efficiency curve for the whole energy range. The deviation for the different curves is little different. Therefore, this uncertainty was generalized to 9% for all the curves over the whole energy range.

7.7 Sum of the uncertainties

The sum of the uncertainties was done for ^{241}Am at 59 keV of energy (Table 11) for the CWT0, using the formula:

$$.u_{tot} = \sqrt{\sum_{i=1}^{N} u_i^2} \qquad \text{(Eq. 11)}$$

Where u_i are the single uncertainties and N is the number of the total uncertainties.

Table 11: Sum of the uncertainties (in the second column the uncertainty was divided for the appropriate distribution coefficient)

Source of uncertainty	Uncertainty	Relative standard uncertainty
Activity	1%	1%
Counting	1%	1%
Repeatability	2%	2%
Distance detector-person	14%	8%
Movement of the person	22%	11%
CWT uncertainties	-24%	-8%
Fitting uncertainties	9%	3%
Sum		16%

Doing the same procedure with the CWT4, we can obtain a sum of uncertainty of 16.5%.

7.8 Other uncertainties with MCNP

7.8.1 Anthropomorphic phantom model

A new voxel anthropomorphic phantom has been used to evaluate the uncertainties of the measurements, since we measure a real person, who is different from a phantom. With this model the objective was to see what happened when the detectors were put in front a real person, who can be really different (fatter, less fat, thinner or less thin) than a "standard man" or than a phantom. This phantom reproduces accurately the organs and the composition of a real man (Figure 7.9).The lungs were filled with a homogeneously distributed source.

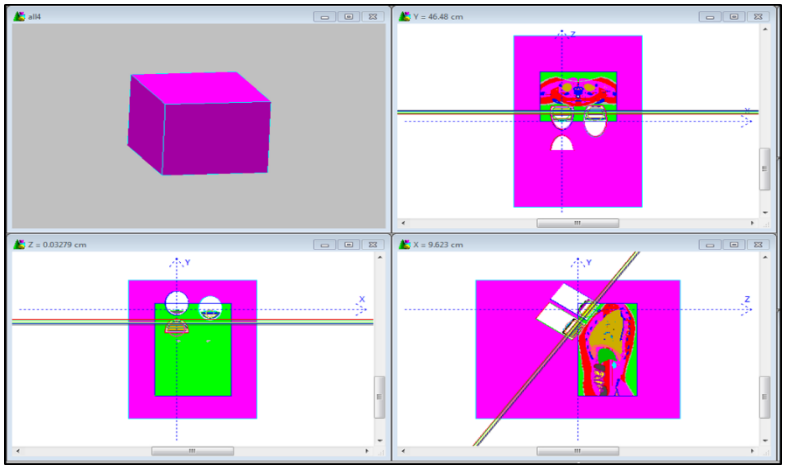

Figure 7.7: view of new phantom from *Moritz*

7.8.2 Validation

Validation of the model was done using measurements with the LLNL phantom. Using the data from the laboratory, it was possible to calculate the CWT of a standard man working in SCK-CEN. This standard man weights about 85 kg, is 1.78 m tall and is 36 years old of average. With the formula (Eq.4), a CWT of 3.4 cm was calculated. So, adding the first overlay to the LLNL phantom, it was possible to reach the required thickness and through the measurements it was possible to see the difference between the

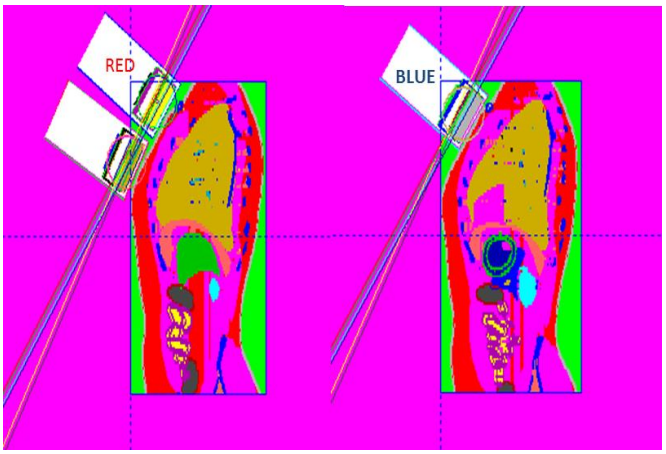

Figure 7.8: validation of the anthropomorphic model

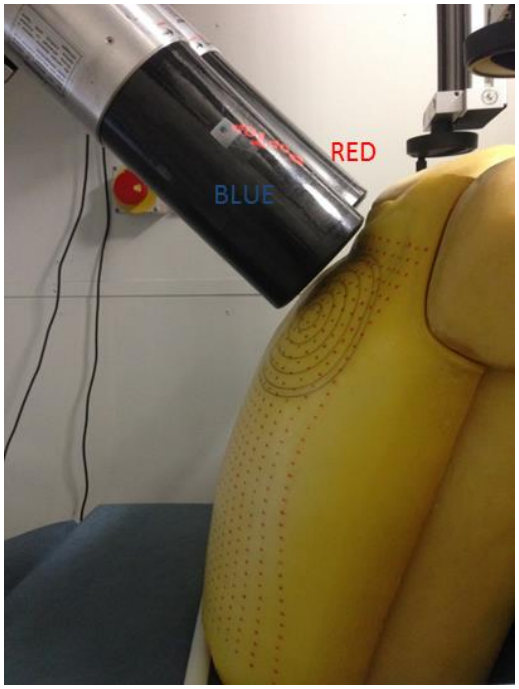

Figure 7.9: position of two detectors for validation

measurements and the simulations. Considering only the Blue and the Red detector we can see an absolute difference of about 13%.

7.8.3 Uncertainties tests

This new phantom was chosen because it is anthropomorphic and it simulates better than LLNL phantom human features This new phantom was used as a test to see how the efficiency could change in two different cases:

- Changing the distance between the chest and the detectors;
- Changing the size of lungs volume.

In the first case, the distance of the detectors from the standard position (1 cm), which is called z in the graph (Figure 7.12) was changed. Four different positions were considered and, as results, it is possible to see that the sum of the efficiency of the tree detectors decreases with 3 (at z-0.5cm position) to 19 % (z-3 cm) (Figure 7.14).
In the second case, the size of the lungs (Figure 7.13) was changed, because everyone has a different size of the lungs, but the activity was the same for all the cases. The phantoms with smaller size of lung was called “thin” and the others with bigger size “fat”. From the graph it is possible to see that, if the size of the lungs is smaller, the efficiency is bigger and it increases up to 70%. This is to be expected, if the lungs are smaller, the source is closer to the detector and, if the real case is considered, the radionuclide is, close to the detector. This can be explained also saying that, for the same activity inhaled, the specific activity is bigger in the case of smaller lungs, but this is not real true, because, in case of inhalation of radioactive material, the person with bigger lungs will inhale more. On the contrary, if we have a person with bigger lungs, it is possible to see a reduction of the efficiency up to 40% (Figure 7.14). The cases considered (the biggest and the smallest) were really extreme.

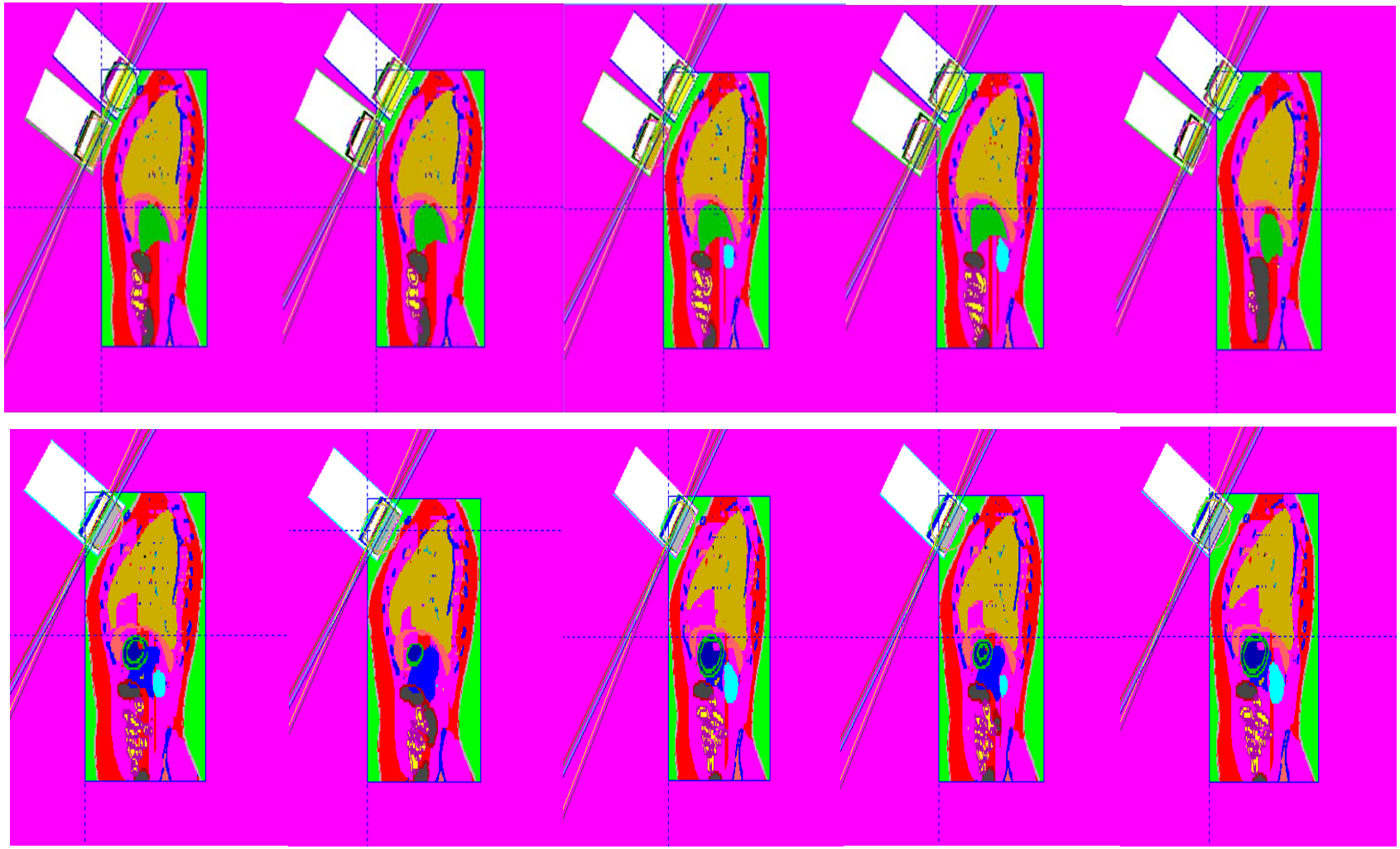

Figure 7.10: change of the distance between the detectors and the chest. Above Red and green detector, below blue detector.

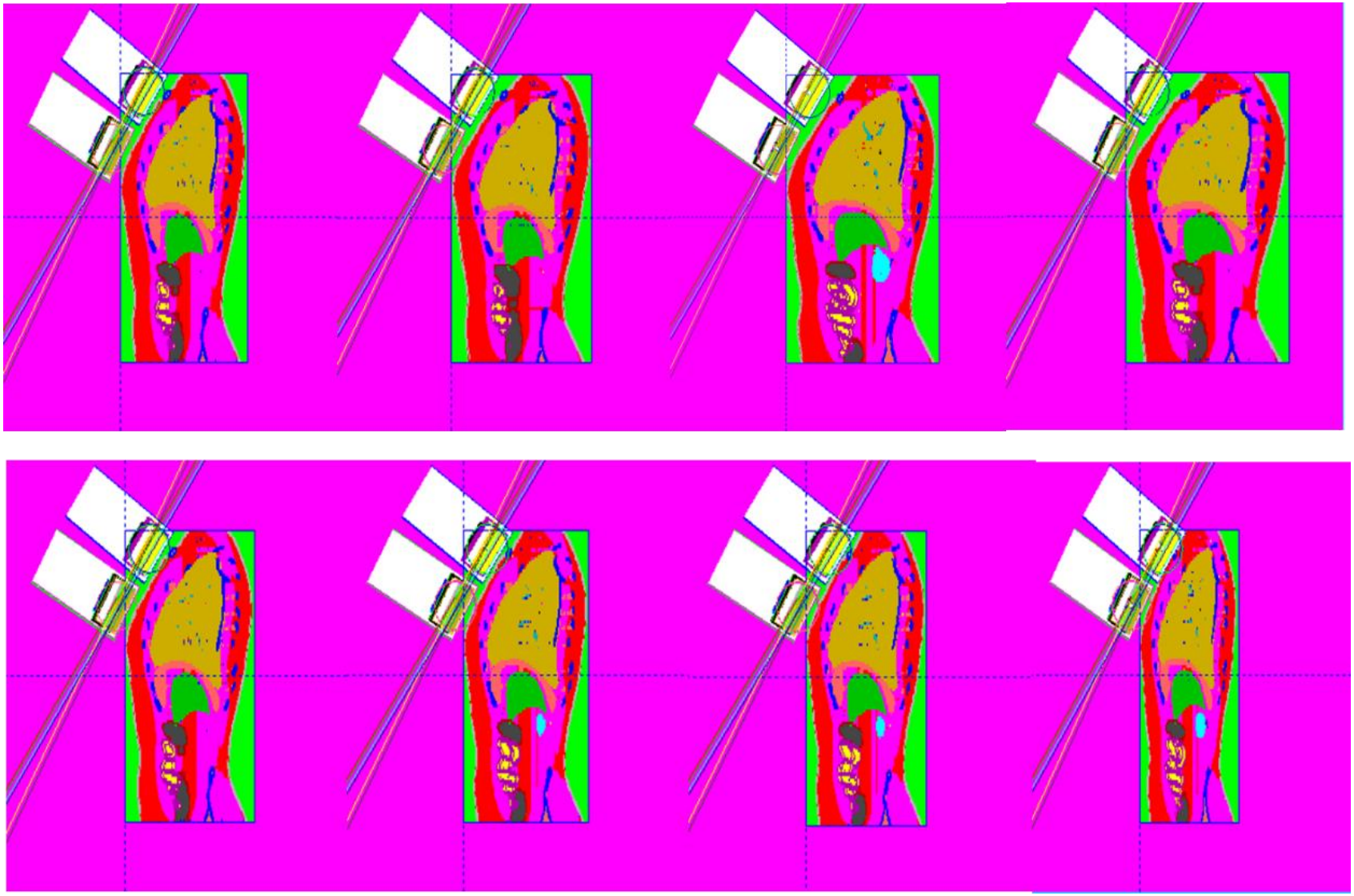

Figure 7.11: change of the lung size. Above the size is bigger, below is smaller

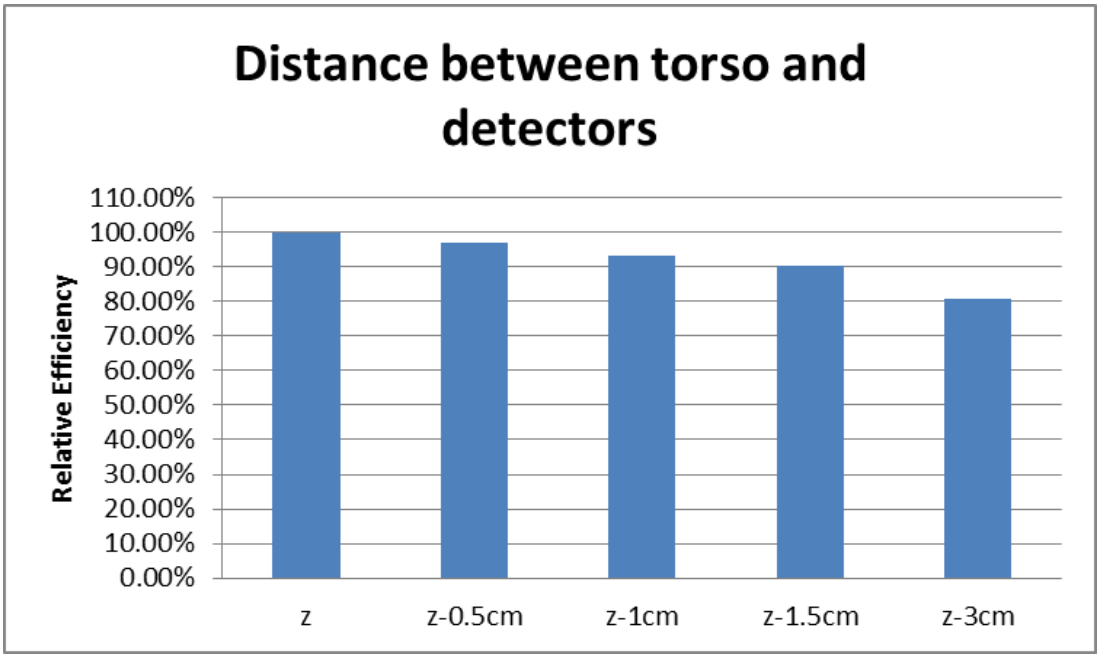

Figure 7.12: relative efficiency changing the distance between detectors and chest

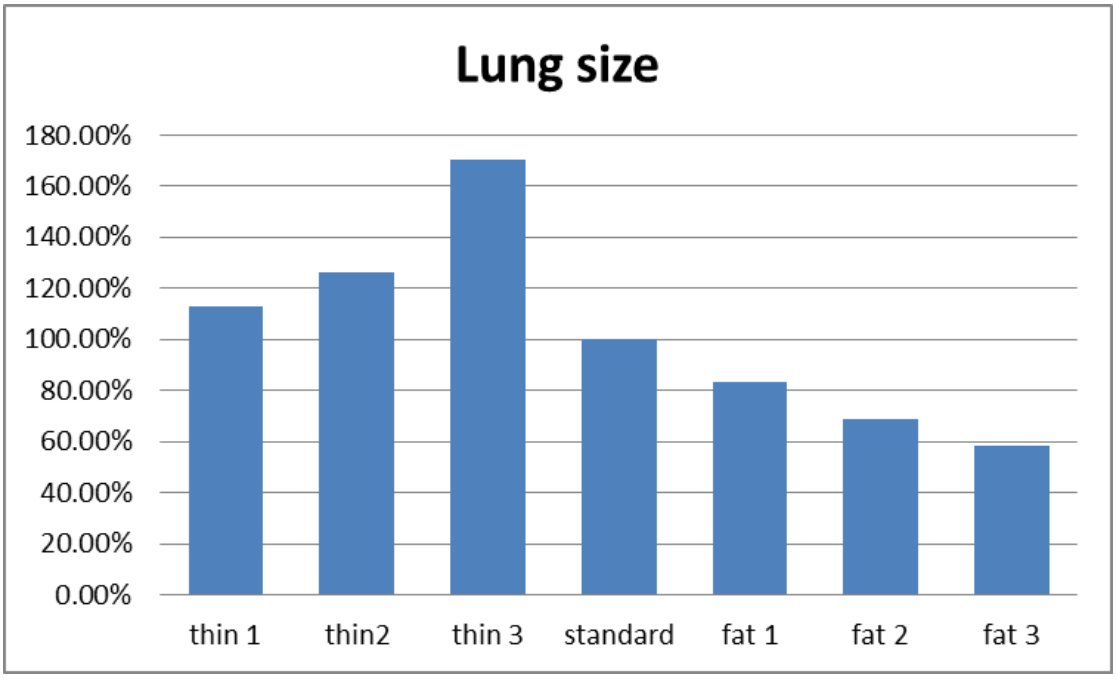

Figure 7.13: relative efficiency changing lungs size

7.9 Detection limits

Detection limits indicate the activity values for which it is possible to detect a false signal at 5% with a confidence level of 95% (or other selected value) or viceversa. This definition of detection limits based on the formalism of Currie [19]
Currie defined measures of detectability and began by defining the concepts of qualitative and quantitative analysis limits. Three limiting levels were defined:

• The critical level L_C, the signal level above which an observed instrument response may be reliably recognized as "detected."

• The detection limit L_D, the true net signal level that may be expected a priori to lead to detection.

• The determination limit L_Q, the signal level above which a quantitative measurement can be performed with a stated relative uncertainty.

Numerical values of these levels depend on four criteria, most importantly the standard deviation of the background. By choosing a probability α (error of the first kind) for falsely deciding that signal is present when in fact it is not, the critical level L_C is calculable. Choosing a probability β (error of the second kind) for deciding that the signal is absent when it is in fact present permits the detection limit L_D to be calculated. Finally, specifying the maximum tolerable statistical error in a quantitative measurement allows the determination limit L_Q to be computed. "The levels L_C, L_D, and L_Q are determined entirely by the error structure of the measurement process, the risks, α and β, and the maximum acceptable relative standard deviation for quantitative analysis. L_C is used to test an experimental result, whereas L_D and L_Q refer to the capabilities of [the] measurement process itself." Currie then gives recipes for calculating these quantities, for the conventional assumptions of a normal distribution; 5 % errors of the first and second kind; the uncertainty of the background independent of the signal level; and quantitation at 10 % or better.

Detection limits are affected by:

- Compton scattering in the person: all gamma radiation coming into the bunker space can be sprinkled on the person and part of it are losing energy. The Compton radiation

that reaches the detector is a continuum in the spectrum over the entire energy range (especially at low energy). The Compton continuum does not equal the background. Indeed, the presence of a person, not only provides more material which can scatter radiations, but it is also an additional source of radiation. The continuum spectrum is also determined by the gamma radiation of the environment (materials of construction of the detector, other materials in the immediate vicinity of the detector, the contribution of natural radioactivity);

- Natural radioactivity measuring: this mainly consists of ^{40}K which increases the spectrum continuum in the area below 1460 keV.
- Presence of radionuclides other than those that it is desired to detect: this generally gives an increased contribution to the continuum if their energy is higher than the energy in which it is desired to calculate a detection limit. This is the case when we want to calculate detection limits for a person who is internally contaminated with other radionuclides. Also medically administered radiopharmaceuticals may increase the continuum spectrum.

For radioactivity or a similar counting measurement, where the data are digital and the distribution Poisson Normal, the equations are particularly simple; for example, if the background is exactly zero with no uncertainty, then L_C = 0 counts, L_D 2.71, and L_Q = 100. In agreement with experience, this means that any observed count will be evidence of a non-zero signal, and 100 counts gives a standard uncertainty of $\sqrt{100}/100$ = 10 %. A more rigorous formulation for L_D, for extreme low-level counting, using the exact Poisson distribution, was given by Currie in 1972. Here, L_D = 3.00 replaces the Poisson-Normal approximation of 2.71 counts [20]

The detection limits will be calculated by using a large number of channels left and right of the position of the peak in order to estimate more accurately the continuum, which allows smaller peaks to be detected. In routine measurements, this method is used for the calculation of the detection limit for ^{241}Am based on the 59.5 keV peak region.

The formula used is [19]:

$$MDA = \frac{4.653 \cdot \sigma_N B + 2.706}{\varepsilon \; I \; t} \qquad \text{(Eq. 12)}$$

Where:

$\sigma_N B$ = standard deviation of the background;

ε = detector efficiency;

I= peak intensity;

t= measurement time.

The Currie formula is implemented inside Genie2000, so by the peak analysis it is possible to find the detection limits and so the MDA (Minimum Detectable Activity).

Testing the new setup by measuring a real person, for a routine measurements of 50 minutes an MDA of 11Bq for the 59 keV peak of ^{241}Am was reported. This value stays in the range of the actual setup (6-18 Bq), but with other measurements with different CWTs it will be possible to find the new range for this setup. This new range is expected lower than the actual one.

CONCLUSIONS

The objective of this study was to calibrate and optimize a new setup for in-vivo lung monitoring in the Anthropogammametry Laboratory at SCK-CEN. This new setup, made of two HPGe, had to be more efficient and more comfortable for the people doing measurements than the actual setup used (two LEGe detectors).

To reach these goals, some background measurements of the bunker and studies of the best position of the detectors had to be done. MCNP code was the tool used to simulate the performances of the detectors in different position to find the one that would give the best efficiency for the measurements. Changing the positions of the detectors with the respect to the phantom (virtual LLNL phantom) allowed to find the best result in terms of efficiency.

After that, efficiency curves depending on the CWT were established through multiple measurements and it is possible to see a really improved efficiency for the energy of interest, almost doubled. Indeed the best result at 59 keV energy, that is the most intense energy peak of ^{241}Am, was searched.

As the calibration was done with a phantom, also the uncertainties in these curves had to be taken into account, because a person is really different from a phantom, either for the composition either because he can move during the measurements (50 minutes). It has been found that the sum of the uncertainties is about 16% (k=1).Other studies of uncertainties were done with MCNP, using an anthropomorphic phantom model. Distance between detectors and torso and size of the lungs were changed to see the efficiency differences. From these studies, the uncertainties found were up to 40% for person with very big lungs.
With this new setup a decrease of MDA it is expected and then improved performances.

Adding a third detector, as planned initially, on the right lung will improve more the efficiency and will decrease the MDA. It was not possible to calibrate this other setup because of a damage of this detector (Loss of vacuum inside the detector). Anyway it is possible that a detector can broke during the time, so the two detector configuration will be useful, because the measurements have to be guaranteed.

Moreover, after the calibration with the third detector and after the implementation for routine lung measurements, these new detectors will be calibrated and used for other scopes, like skull and thyroid measurements and for whole body counting.

References

[1] J. Millman and A. Grabel, *Microelectronics*, McGraw-Hili, Singapore, 1988. (Second Edition).

[2] G. F. Knoll, *Radiation Detection and Measurements*, John Whiley & Sons Inc., 1978 (Third Edition).

[3] "www.orteconline.com/.../High-Purity-Germanium/DetectorManufacturing," Ortec. [Online].

[4] J. Simpson and J. Eberth, "From Ge(Li) detectors to gamma-ray tracking arrays – 50 years of gamma spectroscopy with germanium detectors" from *Progress in Particle and Nuclear Physics 60* , p. 283–337, 2008.

[5] R. H. Pehl. et al., "IEEE Trans. Nucl. Sci." from *NS-26(1),* p. 321, 1979.

[6] T.W. Raudorf. et al., "IEEE Trans. Nucl. Sci." from *NS-31(1),* p. 253, 1984.

[7] ICRP, "Individual Monitoring for Internal Exposure of Workers," ICRP Publication 78. Annals 27 (3-4), 1997.

[8] ICRP, "Human Respiratory Tract Model for Radiological Protection," Pubblication 66, Annals of ICRP 24, No (1-3), 1994.

[9] T. J. Sumerling and S. P. Quant, "Measurement of the human anterior chest wall by ultrasound and estimates of chest wall thickness for use in determination of transuranic nuclides in the lung", from *Radiation Protection Dosimetry* Vol. 3, pag 203-210, 1982.

[10] X-Cooler III Mechanical Cooler for HPGe Detectors, 2012.

[11] "http://www.nucleide.org/Laraweb/," 2016. [Online]. [Accessed 03 may 2016].

[12] Gary H. Kramer and Barry M. Hauck, "The Human Monitoring Laboratory's new lung counter: calibration and comparison with the previous system and the cameco corporation's lung counter" from *Health Physics,* 2005.

[13] R. V. Griffith, P. N. Dean, A. L. Anderson and J. C. Fisher, “Tissue equivalent torso phantom for intercalibration of in vivo transuranic nuclide counting facilities.” from *Report IAEA-SM-229/56,* 1978.

[14] G. H. Kramer and C. E. Webber, “Evaluation of the Lawrence Livermore National Laboratory (LLNL) torso phantom by dosimetry and x-ray.” from *Appl Radiat Isot 43,* 1992.

[15] Denise B. Pelowitz, MCNPX USER'S MANUAL Version 2.7.0, April 2011.

[16] J. F. Briesmeister., “MCNP- A general Monte Carlo code for N-Particle Transport Code Version 4A,” from Los Alamos National Laboratory, Los Alamos, NM, LA-12625-M (UC705 and UC700), Rev.2,1993.

[17] Gary H. Cramer, Paul Crowley and Linda C. Burns, “The uncertainty in the activity estimate from a lung count due to the variability in chest wall thickness profile,” from *Health Physics,* vol. 78(6), pp. 739-743, 2000.

[18] Kenneth. A Van Riper, *Moritz version 1.28,*.White Rock Science

[19] L.Currie, “Limits for Qualitative Detection and Quantitative Determination - Application to Radio Chemistry,” from *Analytical chemistry, Volume 40,* 1968, pp. 586-593.

[20] L. A.Currie, “The Measurement of Environmental Levels of Rare Gas Nuclides and the Treatment of Very Low-Level Counting Data,” from *IEEE Trans. Nucl. Sci. NS19 (1),,* pp. 119-126, 1972.

[21] *Genie 2000* Operation Manual, 2006., Canberra USA

[22] Karen L. Jeffers and David P. Hickman, “Historical review of lung counting efficiencies for low energy photon emitters,” from *www.health-physics.com,* 2014.

[23] E. D. Karachalias, “Master of Science Thesis: Investigation and calibration of various detection systems which can be used for emergency internal contamination checks,” Stockholm, 2013.

ACKNOWLEDGMENTS

I want to thank Anne Laure Lebacq, my mentor in SCK-CEN, for her advices and her support during my internship and also after, during the writing of my thesis. I shouldn't have done my job without the help of Ingrid, the rock of the AGM laboratory, who was like a mom, helping me with the measurements, but also giving me many other advices. I want to thank Pasquale, my "co-supervisors" and office-mate, who was always ready to help me and introduced me to the big world of MCNP. I can not forget about Michel, Eric and Jo; they, in many different ways, helped and supported me. I found a very nice group and I am really glad to have known people like them.
I want to thank my professor, Riccardo Ciolini, who gave me the possibility to start this internship and who supported me especially during the writing, a really hard work for me.

Voglio ringraziare innanzitutto mia madre e mio padre che mi hanno dato la possibilità di iniziare questo lungo cammino di studio e che mi hanno incoraggiato nonostante le difficoltà incontrate, spronandomi a non mollare. Un grazie enorme va a mio fratello Giuseppe che, nonostante sia il più piccolo, sa come farmi ragionare e mi "coccola" nei momenti di bisogno. Un grazie va anche a tutta la famiglia: zii, cugini e nonno e anche a chi purtroppo non c'è più, ma aveva sempre una parola di supporto e di incoraggiamento.
Voglio ringraziare le mie due coinquiline, Stefania e Mari, che sono diventate la mia seconda famiglia a Pisa e senza le quali non sarei riuscita ad arrivare fin qui.
A Fabrizio, come dico sempre, farò una statua, perché un grazie non basta per tutto quello che ha fatto per me. Non posso dimenticarmi di tutte le persone che hanno condiviso questi anni insieme a me, a partire da Michela, con cui ho iniziato questa lunga avventura, passando per Fabio con tutti i suoi consigli e le lunghe chiacchierate ed arrivando a tutti gli altri (che non sto ad elencare, ma sanno bene chi sono) con cui ho passato serate, cene, pranzi, feste e che hanno reso questo cammino più sereno e spensierato. Devo ringraziarli tutti perché so quanto posso essere pesante e stressante a volte.
Alle mie amiche da una vita, Marta e Betta, non posso che dire grazie per la loro amicizia che è durata e continua ad essere sempre la stessa nonostante la lontananza.
Ed infine per ultimo (the last, but not the least) voglio ringraziare tutta la pazza gente del Boeretang, che mi ha fatto passare dei mesi indimenticabili.